ABSTRACT

Title of Dissertation: Piezoelectric MEMS Disk Resonator and Filter Based on Epitaxial $Al_{0.3}Ga_{0.7}As$ Films

Ken Kan Deng, Doctor of Philosophy, 2006

Directed By: Professor Don DeVoe
Department of Mechanical Engineering

In this work, a new class of disk, contour-mode, piezoelectric, micromechanical resonators based on single-crystal $Al_{0.3}Ga_{0.7}As$ films has been developed. The shape of the disk resonator is based on the velocity propagation profile of the elastic wave in the plane of the piezoelectric film, with lateral dimensions scaled to the half wave length of the desired resonance frequency. The resonators are designed with supports to emulate free-free boundary conditions. Finite element analysis (FEA) model for this resonator is created in Ansys software, the simulation results validate the design concept. The performance parameters extracted from the FEA models show that this novel disk resonator outperforms the beam type counterpart. A unique 7-mask MEMS fabrication process based on the epitaxial, heterostructure $Al_{0.3}Ga_{0.7}As$ films has been developed and successfully implemented to produce the prototypes of the new disk resonators. Fully experimental characterizations on the prototypes were conducted and the measured results from the prototypes are: a Q factor of 7031 at 30.2 MHz with 1.11 kΩ intrinsic motional resistance; a Q factor of 6515 at 40.8 MHz with 1.26 kΩ intrinsic motional resistance; a Q factor of 3300 at 62.3 MHz with 2.43 kΩ intrinsic motional resistance. The measured power handling level is about 1.6 mW,

which is the highest power handling capability to date. These measured performance aspects are better than that of the previously developed beam type resonators.

Based on this new disk resonator, two novel, two-port resonators (i.e., filters) designs have been introduced. The FEA models of both designs were created and the simulation results verify these design concepts. Equivalent circuit models for these filters were established with the parameters obtained from the FEA models. Furthermore, the optimal electrode configuration to provide minimum insertion loss is obtained through the analytical transadmittance function of the equivalent circuit. The prototypes of the filters were successfully fabricated. Measured results on these prototypes are summarized here: for the circular patter design, the best insertion loss is -45.7 dB at 37.8 MHz with quality factor 4372; for the half plane electrode design, the best insertion loss is -42.8 dB at 38.1 MHz with quality factor 3632.

Piezoelectric MEMS Disk Resonator and Filter Based on Epitaxial $Al_{0.3}Ga_{0.7}As$ Films

by

Ken Kan Deng

Dissertation submitted to the Faculty of the Graduate School of the
University of Maryland, College Park, in partial fulfillment
of the requirements for the degree of
Doctor of Philosophy
2006

Advisory Committee:

Professor Don DeVoe, Chair/Advisor
Professor Balakumar Balachandran
Professor Teng Li
Professor Bao Yang
Professor Norman Wereley

Dedication

To my wife Dawn Zhai and my father for their support and encouragement in my pursuit of the Ph.D degree.

Acknowledgements

I would like to express my appreciation to Dr. Don DeVoe for his guidance, advice, and support during my study. He also opened a new door for me into the MEMS world. I am grateful to Dr. Parshant Kumar for his excellent work on the device fabrication. I would also like to thank my fellow student, Lihua Li, for her assistance in the prototype measurements. This work is funded by DARPA grant. Finally, I would like to thank the people over in LPS for their support in the device fabrication.

TABLE OF CONTENTS

List of Tables

List of Figures

Chapter 1： Introduction

1.1 Overview of the Field

There is strong demand in the wireless communications industry for highly integrated, low power, and low cost oscillators and high-frequency filters for applications such as mobile phones and GPS receivers. Currently, the discrete BAW (bulk acoustic wave) quartz resonators have been the prevailing choice for such applications because single crystal quartz has very attractive material properties, namely low loss, small temperature coefficient, and low motional resistance. However, the precision discrete quarts resonators for VHF (very high frequency) through UHF (ultra-high frequency) applications are bulky and costly; consequently these drawbacks become the obstacles to produce the low cost, low power, miniature size RF (radio frequency) systems. In the past two decades, microelectromechanical system (MEMS) resonators are being intensively explored as a promising solution to fulfill this need. While dramatic progress has been made, to date there is no ideal solution which can meet all the requirements for communication applications.

Resonators and resonant filters based on capacitively-transduced silicon have been the subject of great attention because they may be incorporated with standard CMOS processing. Furthermore, silicon provides a number of favorable mechanical properties. A wide variety of silicon resonators based on bending-mode and longitudinal-mode planar 1-D or 2-D radial-mode designs have been described [1-6].

From the application perspective, there are five important metrics which specify resonator performance, namely: maximum resonance frequency (f_r), minimum series motional resistance (R_x), maximum quality factor (Q), and maximum power-handling ability, and stability [1]. By taking advantage of the low material losses inherent in both single crystal silicon and polycrystalline silicon, bending-mode capacitive resonators with high Q have been demonstrated. For example, Wang et al [2] achieved a Q over 10,000 at around 100 MHz in vacuum for a bending-mode beam with free-free boundary conditions. In contrast to such bending-mode designs, planar resonators offer the benefit of higher stiffness and lower viscous damping when operating in air. The highest product of frequency f_o and quality factor Q reported for a microresonator in air is a planar-mode device with $f_rQ = 3.88\text{x}10^{12}$ [1]. In addition, 2-D planar-mode resonators tend to offer better power handling capability than bending-mode designs. A single crystal silicon planar resonator with a maximum power handling level up to 0.12 mW at 13.1 MHz was recently described [3]. Although this remains the highest power handling level reported for a capacitive resonator, it is still lower than wireless communication requirements on the order of several mW based on typical incident power levels as well as phase noise limitations [7]. Another drawback of capacitive resonators is that they require extremely small capacitive gap spacing on the order of 100nm or below to provide sufficient electromechanical coupling strength. This requirement can introduce substantial fabrication complexities. To further increase the electromechanical coupling strength and thereby lower the series motional resistance, R_x, high bias voltages (>10V) are generally required, introducing an additional limitation. For example, a motional

resistance of only 1.46 kΩ was reported for an electrostatic resonator with an 80 nm capacitive gap and 12V bias voltage [2]. Upon increasing the gap to 160 nm, the fabrication requirements are relaxed, but motional resistance is sacrificed, with an R_x of 43.3 kΩ under17 V bias potential reported [1].

Compared to capacitively-transduced resonators, MEMS resonators based on piezoelectric transduction can potentially offer a number of advantages. Due to the inherently linear nature of piezoelectric transduction, rather than the quadratic relationship in electrostatic coupling, piezoelectric-based microresonators can handle substantially higher power levels. Because piezoelectric transduction is based on absolute strain rather than relative displacement, high electromechanical coupling can be realized without resorting to nanoscale gaps, resulting in simpler design and implementation. Furthermore, the electromechanical transduction coefficients for many piezoelectric materials provide more effective coupling than capacitive transduction, offering low values of motional resistance R_x without the use of large bias voltages. Many piezoelectric materials used for MEMS resonators exhibit higher internal losses compared to silicon. Furthermore, the piezoelectric film must be sandwiched between conductive electrodes to apply the electric field and sense the electric charge produced at resonance. However, metal electrodes tend to exhibit high levels of thermoelastic damping, and can reduce the overall Q of a resonator by an order of magnitude of more [8, 9]. Consequently, relatively low quality factor Qs have been reported in several previous efforts at demonstrating piezoelectric microresonators [10, 11].

A number of planar-mode piezoelectric resonator designs have recently been demonstrated [12-15], with superior performance over their bending-mode counterparts. Li et al. demonstrated extensional-mode bar resonators operating up to 25 MHz with Qs as high as 25,390 and motional resistance between 4-18 k [15], and Piazza et al. presented a ring-shaped piezoelectric contour-mode resonator with a quality factor of 2,900 at 472.7 MHz and motional resistance around 2.6 k based on their reported admittance plots [13]. Despite these advances, relatively little effort has been spent on planar piezoelectric microresonators, in part because of the difficulty in integrating high quality single-crystal piezoelectric materials and lack of an effective design methodology to accommodate the anisotropy inherent in these materials.

Epitaxially grown III-V materials are widely used for the production of high speed VLSI circuits. With the exception of AlN, the use of the piezoelectric effect in III-V materials has received little attention. Recently, a fabrication process [16] for realizing bending-mode and longitudinal-mode [17] resonators based on single-crystal piezoelectric $Al_{0.3}Ga_{0.7}As$ combined with Si-doped $Al_{0.3}Ga_{0.7}As$ electrodes has been reported by our group. The lattice-matched single-crystal heterostructure essentially eliminates residual stress-induced curvature. This is an important consideration for the planar disk resonators, since any out-of-plane curvature will have a deleterious effect on quality factor due to excitation of spurious out-of-plane modes. In addition, the $Al_{0.3}Ga_{0.7}As$ heterostructure exhibits relatively low material damping compared to traditional devices using polycrystalline piezoelectric films

such as PZT, ZnO, or AlN combined with metal electrodes. The use of $Al_{0.3}Ga_{0.7}As$ for the resonator structure also holds promise for future integration with high-speed III-V electronics.

1.2 Dissertation Objectives

To step up from the conventional beam resonator design, the development of a new 2-D (two-dimensional), planar mode, disk resonator technology based on epitaxially-grown, single-crystal AlGaAs films is described in this dissertation. The planar extensional mode is chosen in this effort rather than the film thickness modes, because planar modes provide the design flexibility for resonance scaling by taking advantage of precision photolithography, and eliminating film thickness variation-induced performance degradation while totally decoupling the film thickness from the mechanical resonance. However, single-crystal AlGaAs films possess cubic symmetry and exhibit orthotropic elastic behavior. Traditional design approaches for isotropic piezoelectric materials cannot be employed since acoustic propagation speed is a function of the crystal orientation. Therefore, a new design methodology is developed. A properly designed 2-D piezoelectric resonator can trap maximum energy and exclude other spurious oscillating modes. It is believed that the new 2-D resonator can ultimately provide better performance over bending-mode designs. To gain insight and extract the parameters of the 2-D resonator, the analysis of a finite element model for this resonator is described. The finite element analysis (FEA) model can predict resonant mode shapes, resonance frequencies, etc. With the

customized algorithms, the parameters of the equivalent circuit are also extracted from FEA results.

In order to achieve the highest Q factor in the 2-D disk resonator, the energy dissipation mechanisms in the resonator system have to be well understood. While there are many energy dissipation paths in the developed microresonators, the most important energy damping mechanisms are identified and the quantitive analyses on the energy dissipations are conducted. The estimated Qs from these analyses serve to define the upper limit of the achievable quality factor for this resonator system. These resonator damping modeling and calculations can also assist in optimizing device design.

To realize the planar AlGaAs design, a feasible MEMS fabrication process was developed. The previously process [16] developed by our group, which is tuned for the production of the beam type AlGaAs resonators, was further optimized and adapted for the disk resonators. In particular, the problem of large parasitic capacitance was addressed. It is well-known that in a RF resonator, large parasitic impedances can distort the response and impair performance. For instance, large feedthrough capacitance can lead to substantial degradation of the resonator SNR. The goal for the fabrication development is to be able to produce working prototypes of the 2-D disk resonators, and use these prototypes to verify theoretical performance.

Bandpass filter is another indispensable component in radio communication systems. In RF transceiver systems, filters with low insertion loss and high quality factors can protect receivers from adjacent channel interference and limit the bandwidth of transmitter noise. Disk resonators employing a 2-port configuration are explored in this work for application to bandpass filters. An equivalent circuit model which describes the 2-port devices is developed, and the analytical transfer function of this filter topology is derived from the equivalent circuit with the aid of the electric network theory, enabling the performance characteristics of the novel filters to be studied. In particular, the optimal electrode layout is determined. Prototypes of the filters with different electrode patterns have been fabricated and tested.

1.3 Dissertation Organization

In the first chapter, an overview of the field of MEMS resonator is provided, the motivations behind our choice of the single crystal AlGaAs 2-D resonator are discussed, and the overall objectives of this dissertation are presented. In the following chapter, the piezoelectric and elastic properties of the eptitaxial AlGaAs single crystal films are described, then the general acoustic wave propagation speeds in any directions in the (100) plane are calculated. A new disk resonator design is proposed based on the profile of the acoustic wave speed. This new class of resonator is then characterized by FEA model in ANSYS. In Chapter 3, details of the fabrication processes used to realize prototype 2-D $Al_{0.3}Ga_{0.7}As$ resonators based on reactive ion etching (RIE) combined with wet release etching are presented. A method to eliminate the capacitive coupling between the top and bottom electrodes of the contact pad area is successfully established. It is featured by the paralene filled

isolation trench and the metallic film jump bridge. In Chapter 4, the major damping mechanisms in this resonator system are identified and modeled. First-order estimations of the Q factors with respect to each damping mechanism are given. Furthermore, the total Q factors of the disk resonators at different geometries are derived. The measured performance of the fabricated prototypes is presented in Chapter 5, and compared to the theoretical and FEA results. In chapter 6, the design of a 2-port disk resonator is presented as an element for a MEMS bandpass filter. The equivalent circuit of the two-port resonator is derived. By employing this model, optimal electrode layouts are determined. The measured performances of the fabricated filters are presented and used to verify the theoretical model. Finally, in Chapter 7, a discussion of the results from this work is presented, and the future directions for impedance matching of the standard 50 Ω RF systems and for further performance improvement the AlGaAs disk resonator are proposed.

Chapter 2 : Disk Resonator Design

2.1 Introduction

The class of III-V materials has many interesting properties. Besides well-known merits such as large band gap and high electron mobility, which have been extensively exploited in a variety of high speed ICs, many other physical properties like piezoelectric, piezoresistive, piezooptic, etc. have been reported, and the potentials for these materials in a myriad of MEMS devices have been discussed [18, 19]. In particular, single crystal heterostructures fabricated from multiple layers of $Al_xGa_{1-x}As$ layers are attractive for MEMS applications since the lattice constants of this family are nearly identical, and aluminum and gallium atoms are easily substituted in the lattice without causing too much strain in the film. Today, the epitaxy techniques have matured and high quality $Al_xGa_{1-x}As$ films can be repeatedly and precisely grown. Most of the previously developed MEMS devices utilizing III-V materials are in the form of one-dimensional (1-D) beam elements [20, 21], in part because the 1-D beam model is easy to analyze and the direction of the beam can be chosen along the maximum transduction direction of the single crystal material. Recently, a fabrication process [16] for realizing bending-mode [22] and longitudinal-mode [15] resonators based on single-crystal piezoelectric $Al_{0.3}Ga_{0.7}As$ combined with Si-doped $Al_{0.3}Ga_{0.7}As$ electrodes has been reported by our group.

From the published literatures, it has shown that 2-D devices are more efficient than the 1-D counterparts and have better performance [23]. However, traditional design

approaches for isotropic piezoelectric material can not be employed in the design of 2-D AlGaAs devices due to the highly anisotropic nature of the crystal structure. Specifically, both the acoustic propagation speed and piezoelectric constants are functions of the crystal orientation. In this work, a new method for designing a 2-D planar-mode, piezoelectric resonator or filter is developed. This approach is based on the well understand of the elastic and piezoelectric properties of this family of single crystal materials, i.e., $Al_xGa_{1-x}As$ epitaxial films. In the following section, the material properties of epitaxial $Al_xGa_{1-x}As$ are discussed. The material properties in any directions are obtained from the correspondent material tensor rotations. The piezoelectric acoustic speeds in the $Al_{0.3}Ga_{0.7}As$ plane are then calculated. The appropriate shape of the 2-D resonator is derived from the radial elastic wave velocity profile, with radial dimensions set to the half wave length of the designated resonant frequency. This configuration ensures a pure planar resonant mode while suppressing other spurious modes. In the last section, finite element analysis (FEA) using Ansys software is conducted. The FEA models not only help to verify the new design approach, but also provide a powerful design tool which can retrieve the performance parameters of the resonator and help to identify better anchoring designs. The simulated results shows that both Q and R_x are greatly improved compared with equivalent longitudinal-mode beam resonators. In Chapter 6, the measured results are compared against these theoretical and simulated results and show good agreements with them.

2.2 $Al_xGa_{1-x}As$ Crystal Properties

The III-V family of materials possesses a cubic zincblende structure (group 43m). The single crystal $Al_{0.3}Ga_{0.7}As$ films used in this study are grown by molecular beam epitaxy on (100) GaAs wafers. The crystallographic coordinate of the $Al_{0.3}Ga_{0.7}As$ crystal in this situation is shown in Figure 2.1, and theoretical piezoelectric (d), orthotropic elastic stiffness (C), and relative dielectric constant (ε) matrices of this crystal are given as:

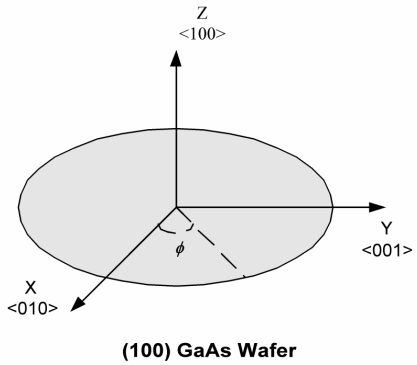

Figure 2.1: Crystallographic coordinate of $Al_xGa_{1-x}As$ crystal in the plane of (100)

$$d = \begin{bmatrix} 0 & 0 & 0 & -d_{14} & 0 & 0 \\ 0 & 0 & 0 & 0 & -d_{14} & 0 \\ 0 & 0 & 0 & 0 & 0 & -d_{14} \end{bmatrix}$$

$$C = \begin{bmatrix} C_{11} & C_{12} & C_{12} & 0 & 0 & 0 \\ C_{12} & C_{11} & C_{12} & 0 & 0 & 0 \\ C_{12} & C_{12} & C_{11} & 0 & 0 & 0 \\ 0 & 0 & 0 & C_{44} & 0 & 0 \\ 0 & 0 & 0 & 0 & C_{44} & 0 \\ 0 & 0 & 0 & 0 & 0 & C_{44} \end{bmatrix}$$

$$\varepsilon = \begin{bmatrix} \kappa & 0 & 0 \\ 0 & \kappa & 0 \\ 0 & 0 & \kappa \end{bmatrix} \tag{2.1}$$

where: $d_{14} = 2.69+1.13x$ *(pC/N);*

$C_{11}=118.8+1.4x$ *(GPa);* $C_{12}=53.8+3.2x$ *(GPa);* $C_{44}=59.4-0.5x$ *(GPa);*

$\kappa = 10.89-2.73x$;

x is the Al mole fraction (0<x<1).

Also, the general density of $Al_xGa_{(1-x)}As$ alloy is given by: $\rho = 5360 - 1600x$ *(kg/m^3)*

Within the $Al_{0.3}Ga_{0.7}As$ crystal plane, both mechanical and piezoelectric properties vary with crystal direction. To obtain these properties, rotation of property tensors is required. Using the indicial tensor notation, the transformed stiffness tensor (C_{ijkl}) and piezoelectric tensor (d_{ijk}) can be found from the original tensors for an arbitrary azimuthal angle ϕ as [24],

$$C'_{ijkl} = \alpha_{im}\alpha_{jn}\alpha_{ko}\alpha_{lp} \cdot C_{mnop} \tag{2.2}$$

$$d'_{ijk} = \alpha_{im}\alpha_{jn}\alpha_{ko} \cdot d_{mno} \tag{2.3}$$

where: index i,j,k,l,m,n,o,p =1,2,3;

α_{xy} is direction cosine determined from the direction cosine matrix,

$$\alpha = \begin{bmatrix} 0 & \cos(\phi) & \sin(\phi) \\ 0 & -\sin(\phi) & \cos(\phi) \\ 1 & 0 & 0 \end{bmatrix} \tag{2.4}$$

Using Matlab, the above rotation calculations were performed within the film plane, with the results shown in Figure 2.2 and 2.3. As shown in Figure 2.3, the transverse piezoelectric coefficient d_{31} reaches its maximum value 3.0 pC/N in <011> direction as the shear piezoelectric coefficient d_{36} diminishes to zero at this direction, while in <001> direction d_{36} achieves its maximum value 3.0 pC/N and d_{31} drops to zero.

Ideal isotropic materials should have a circular pattern in the property polar plots. Apparently, $Al_{0.3}Ga_{0.7}As$ crystal is very anisotropic both in elastic stiffness and in piezoelectric transduction. Most beam type devices are aligned with the <011> direction so that the maximum d_{31} is realized. For an extensional mode $Al_{0.3}Ga_{0.7}As$ beam, if its width is too large, the other twisting or flexural modes will be introduced and its performance is deteriorated.

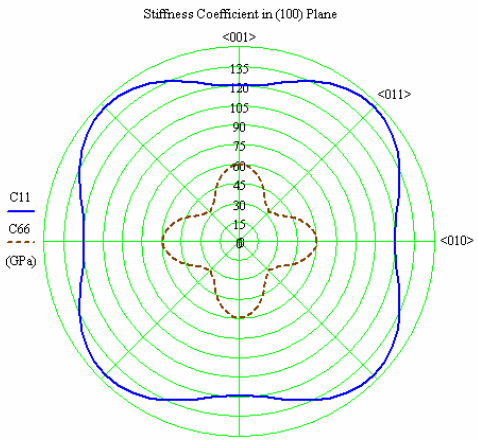

Figure 2.2: Stiffness coefficients C_{11} and C_{66} in (001) $Al_{0.3}Ga_{0.7}As$ plane

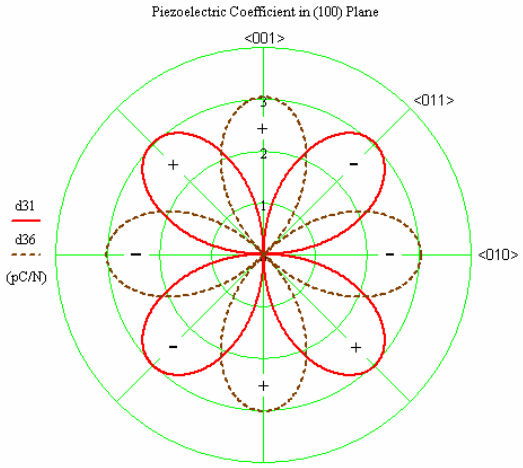

Figure 2.3: Piezoelectric coefficients d_{31} and d_{36} in (001) $Al_{0.3}Ga_{0.7}As$ plane

2.3 Elastic Wave Propagation Speed and 2D Resonator Profile

In this section, the elastic wave propagation speeds in all directions in (100) plane of $Al_{0.3}Ga_{0.7}As$ are calculated based on the material properties obtained above. For free vibrations, the wave equation that describes elastic waves in an anisotropic elastic medium is as following,

$$\rho \frac{\partial^2 u_i}{\partial t^2} = \frac{\partial \sigma_{ij}}{\partial x_j} \tag{2.5}$$

where: index i,j = 1,2,3;

u_i component of displacement vector;

σ_{ij} stress tensor.

The waves propagating in a piezoelectric crystal are really a combination of elastic and dielectric polarization modes. The constitutive equations of a piezoelectric material are given as:

$$\sigma_{ij} = C_{ijkl} \cdot u_{kl} - e_{kij} \cdot E_k$$

$$D_i = \varepsilon_{ij} \cdot E_j + e_{ijk} \cdot u_{jk} \tag{2.6}$$

where: tensor index $i,j,k,l = 1,2,3$;

C_{ijkl} elastic constants;

u_{ij} strain tensor and $u_{ij} = \frac{1}{2}\left(\frac{\partial u_i}{\partial x_j} + \frac{\partial u_j}{\partial x_i}\right)$;

e_{kij} piezoelectric tensor and related to d_{ijk} tensor by $e_{ijk} = d_{imn} \cdot C_{mnkl}$;

E_k electric field;

ε_{ij} dielectric constant;

D_i electric displacement;

In equation (2.5) and (2.6), the summation convention for repeated indices is used. The electric field E_k can be expressed as the gradient of a scalar potential ϕ: $E_k = -\frac{\partial \phi}{\partial x_k}$. Also, according to the Maxwell equation, one has: $D_{i,i} = 0$.

Note that the tensor forms are employed in the above equations instead of the compact matrix forms, since the tensor representation can be transformed as coordinate transforming. Assume the propagating plane waves have the following solution forms

$$u_i = \alpha_i \cdot e^{i\frac{2\pi}{\lambda}(b_i x_i - vt)}$$

$$\phi = \alpha_4 \cdot e^{i\frac{2\pi}{\lambda}(b_i x_i - vt)} \tag{2.7}$$

where: b_i are direction cosines and satisfy the relation, $b_1^2 + b_2^2 + b_3^2 = 1$;

v is the phase velocity (speed);

λ is the wavelength.

Note in solution (2.7), the direction of wave propagation is defined by the vector $\boldsymbol{k} = (b_1,b_2,b_3)$. Now substitute solution (2.7) into equation (2.5) and (2.6), after successive algebraic operations, the following equation is obtained:

$$(\Gamma_{ij} - \rho \cdot v^2 \cdot \delta_{ij}) \cdot \alpha_i = 0 \qquad (2.8)$$

where:
$$\Gamma_{ij} = \left[C_{ijkl} + \frac{e_{mij} \cdot e_{mkl} \cdot b_m \cdot b_n}{\varepsilon_{rs} \cdot b_r \cdot b_s} \right] \cdot b_i \cdot b_l \qquad (2.9)$$

The set of quantities Γ_{jk} form a rank 2 tensor or Christoffel tensor. Equation (2.8) is an eigenvalue problem of the Christoffel tensor [25]. The eigenvalues of Γ_{jk} are directly related to the three wavespeeds, with one corresponding to the wave parallel to $\boldsymbol{k}$ (longitudinal wave), and the other two are corresponding to the waves perpendicular to $\boldsymbol{k}$ (transverse or shear waves).

In the plane of (100) $Al_xGa_{(1-x)}As$ crystal plate, the direction vector $\boldsymbol{k}$ has the format of ($\cos\phi$, $\sin\phi$, 0). The material properties given by (2.1) are in matrix formats. In order to apply formula (2.9), one has to convert them into tensor formats, and the index conversions follow the transformation rules given in the table below [24].

Table 2.1: Correspondent indices between matrix and tensor

Tensor indices	11	22	33	23, 32	31,13	12, 21
Matrix indices	1	2	3	4	5	6

Once the tensor forms of AlGaAs properties are known, the formula (2.9) can be applied. Using Matlab, the velocities of wave propagation were calculated from equations (2.8), (2.9) (The Matlab program is given in Appendix A). The results are presented as a function of azimuthal angle ϕ in the (100) plane in Figure 2.4. The longitudinal elastic wave speed in this figure is of particular interest for the disk resonator design. Unlike an in-plane isotropic material, whose speed profile is an ideal circle, the $Al_{0.3}Ga_{0.7}As$ crystal has a speed profile similar to a rounded square due to the inherent material anisotropy.

An ideal, longitudinally vibrating, piezoelectric plate should have the same profile as the velocity profile of its elastic wave propagation to ensure a pure resonating mode with spurious modes excluded. When the longitudinal, fundamental mode of a boundary-free plate is excited at resonance, a standing elastic wave is created when the radial dimensions are equal to the half wavelength of the resonance frequency. Inspired by this concept, a new design methodology for a disk-shaped planar resonator is proposed in which the free boundary of the 2-D resonator is shaped proportional to the profile of elastic wave propagating speed, and then scaled to set its radial dimensions equal to the half wave length of the desired resonating frequency, i.e.,

$$R_k = \frac{v_k}{2 \cdot f_r} \tag{2.10}$$

where: R_k is the radial dimension;

v_k is the elastic wave propagating speed in same direction;

f_r is desired resonant frequency.

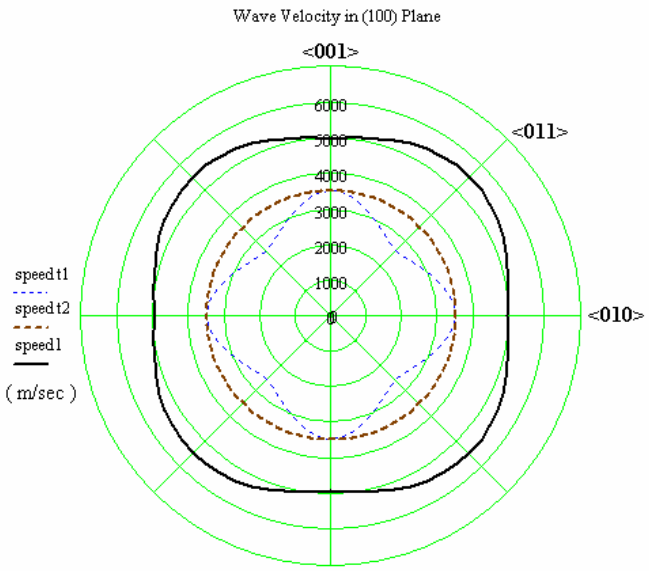

Figure 2.4: Velocity of wave propagation in $Al_{0.3}Ga_{0.7}As$ (001) plane

2.4 Finite Element Analysis and Parameter Extraction

2.4.1 Modal analysis and resonator working mode

To verify the design concept and gain more insight to the planar disk resonator, a finite element model was created in ANSYS 8.0. In this model, the piezoelectric 3-D element SOLID98 was used for the piezoelectric material, with $Al_{0.3}Ga_{0.7}As$ properties given by equation (2.1). For this simulation, continuous electrodes are applied to the top and bottom surfaces of the piezoelectric plate. Modal analysis was conducted to determine resonant frequencies and mode shapes for a 5 μm thick resonator with lateral dimensions varying between 80 um in the <001> direction and 89 μm in the <011> direction. The first three in-plane vibration modes resulting from this analysis are shown in Figure 2.5.

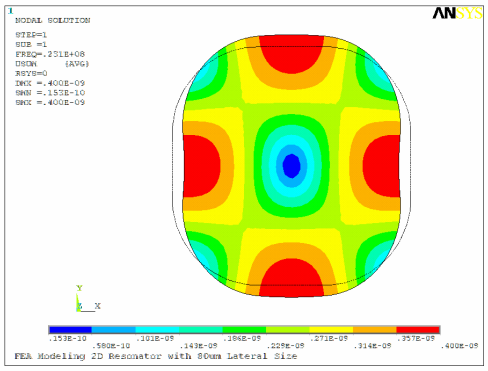

a) Mode 1, f_r = 23.1 MHz

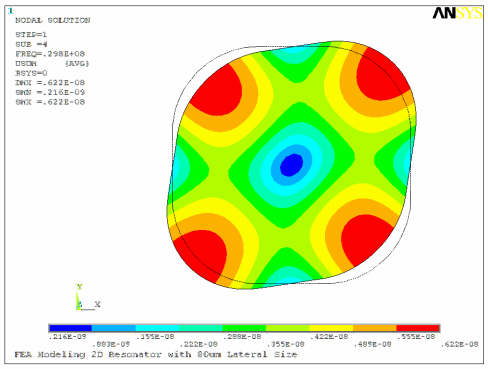

b) Mode 2, f_r = 29.8 MHz

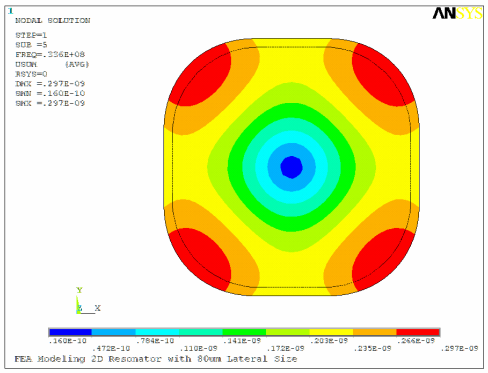

c) Mode 3, f_r = 33.6 MHz

Figure 2.5: Displacement contours of the first 3 in-plane resonant modes predicted by FEA model

However, when the plate is actuated by applying an electric field between the top and bottom electrodes, modes 1 and 3 will not be excited. This observation results directly from the form of the piezoelectric matrix in equation (2.1), which dictates that only shear strains are generated upon application of an electric field across the thickness

(z-axis) of the resonator. Since modes 1 and 3 are excited only by normal strains in the <001> directions, these modes are suppressed for the chosen resonator geometry. Thus the undesired modes are effectively eliminated as a direct result of the AlGaAs anisotropy and proposed design approach. This can be further validated by observing the electrical admittance spectrum of the resonator. The admittance predicted from the finite element model for a 1 V amplitude sinusoidal voltage applied to the top electrode is shown in Figure 2.6. Only one resonant peak is visible in this figure, at a frequency (29.8 MHz) very close to the predicted 2nd mode frequency (30.8 MHz), while the predicted 1st and 3rd modes do not appear at all. This phenomenon is also verified by the experimental results from the built prototypes. Figure 2.7 shows the measured impedance response vs. frequency, i.e., transmission response, in the range of 20 MHz to 35MHz. Clearly, only one peak shows in this measured curve and the correspondent frequency of the peak is 30.1 MHz, which is very close to the FEA as well as the theoretical predicted resonance frequency.

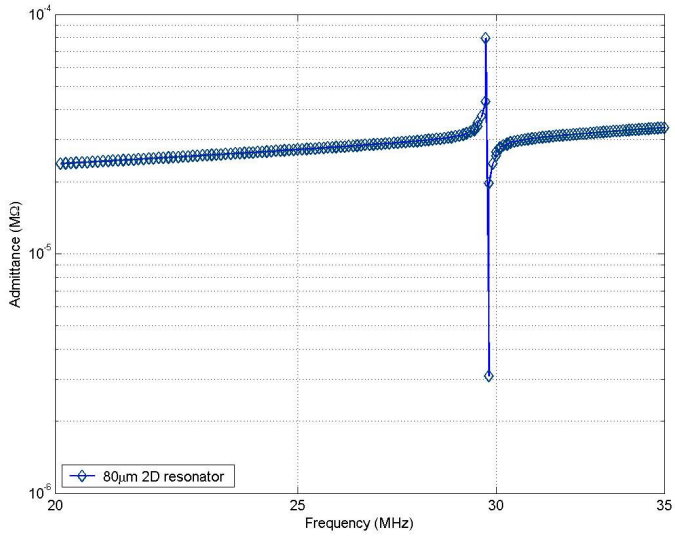

Figure 2.6: Simulated admittance spectrum for an 80μm disk resonator

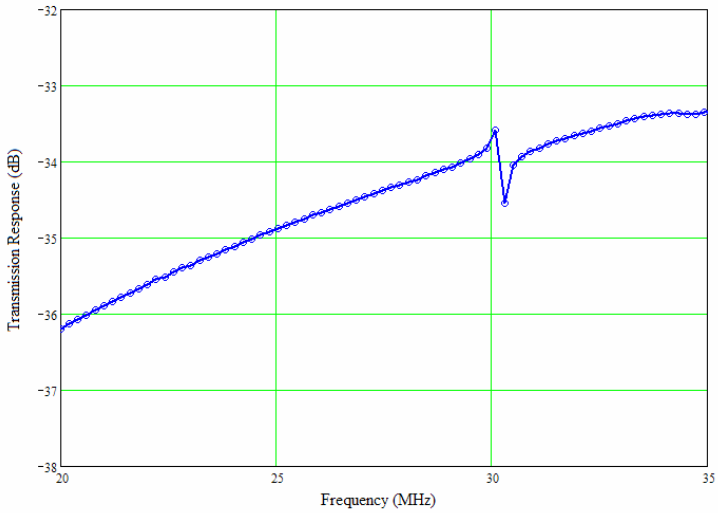

Figure 2.7: Measured transmission response of the 80μm disk resonator prototype

The fact that the antisymmetric <011> breathing mode shown in Figure 2.5 (b) is the only mode to appear in the spectral response offers another practical benefit. Because this mode possesses 4 nodal points where the disk boundary intersects the <001> axes, the anchors may be placed at these points rather than the center of disk, enabling anchor losses to be minimized in a manner which is compatible with the AlGaAs microfabrication process. Figure 2.8 shows the working mode of the 80 μm disk resonator with 2 support beams. The FEA results indicate that this support structural design has minimum effect on the disk resonator performance. Nevertheless, the energy loss through the support beams is thoroughly studied in the later chapter.

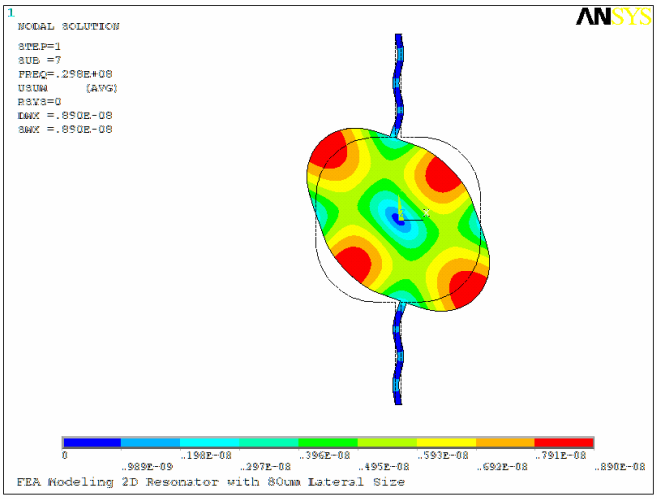

Figure 2.8: Working mode shape of the 80 μm disk resonator with dual support beams

2.4.2 Parameter extraction and motional resistance

A piezoelectric resonator can be modeled by an equivalent circuit shown in Figure 2.9. The lumped elements: *Me, Ke, and Ce* represent the modal mass, modal stiffness, and modal damping of the operational resonant mode, respectively. These lumped mechanical components are coupled to the electric domain through an ideal transformer with a transduction coefficient η. This circuit can be further simplified by removing the transformer and forms the well known Butterworth-Van Dyke equivalent circuit, which is shown in Figure 2.10.

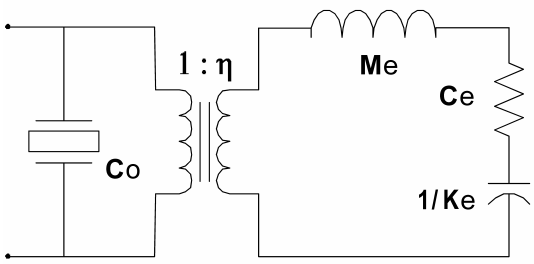

Figure 2.9: Equivalent circuit for a piezoelectric resonator

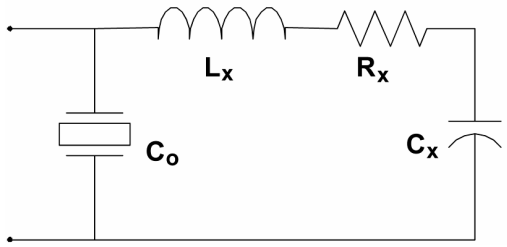

Figure 2.10: Butterworth-Van Dyke equivalent circuit for a piezoelectric resonator where: $Lx=Me/\eta^2$, $Cx=\eta^2/Ke$, $Rx=Ce/\eta^2$

The resistor R_x, also called motional resistance, is the most important parameters for a resonator. Since, it determines the resonator impedance at resonance, and is directly related to the quality factor Q of a resonator by:

$$Q = \frac{L_x \cdot \omega_r}{R_x} \tag{2.11}$$

where: $\omega_r = \sqrt{L_x \cdot C_x}$ is the resonance frequency.

The algorithms are developed to derive M_e, C_e, K_e, and η based on the FEA modal analysis results. And they are listed below:

- Effective mass M_e calculation

$$Me = \int_V \Phi^2 \cdot \rho \cdot dV = \sum_{element\ i} m_i \cdot d_i^2 \tag{2.12}$$

where: Φ is the mode shape function;

m_i is the element mass;

d_i is the element displacement.

- Effective stiffness K_e calculation

$$K_e = \omega_r^2 \cdot M_e \tag{2.13}$$

- Damping coefficient C_e calculation

$$C_e = \frac{\omega_r \cdot M_e}{Q} \tag{2.14}$$

The quality factor Q is obtained through measurement

- Electromechanical transduction coefficient η calculation

$$\eta = \frac{I(j\omega)}{V(j\omega)} = \frac{\int_A d_{ikl} T_{kl} \cdot j\omega \cdot dA}{d_{\max} \cdot j\omega} = \frac{\sum_{element\ i} d_{36} \cdot \sigma_{xy\ i} \cdot dA_i}{d_{\max}} \tag{2.15}$$

where: $\sigma_{xy\ i}$ is the i[th] element shear stress;

d_{36} crystal shear piezoelectric coefficient (refer to equation (2.1));

dA_i is the i[th] element area on electrode;

d_{max} is the maximum displacement of the mode shape.

Once the mechanical lumped components: *Me, Ke, Ce*, and η are known, then the values of electric components: *Lx, Cx, Rx* can also be decided. The resonator with the lateral size of 80 μm is chosen as the calculation example. All the extracted parameters of this resonator from equation (2.12)-(2.15) are listed in Table 2.2.

Table 2.2: Extracted Parameters of the 80 μm $Al_{0.3}Ga_{0.7}As$ disk resonator

Resonator Type		**80 μm Disk**
Resonance Frequency		29.8 MHz
Quality Factor *Q* *(measured in air)*		6,500
Mechanical Parameters	Effective Mass *Me*	6.13 x10^{-5} mg
	Effective Stiffness *Ke*	2.149 x10^{6} N/m
	Damping Coefficient *Ce*	1.77 x10^{-6} N/m/sec
Electromechanical Transduction Coefficient η		2.86 x10^{-5} N/volt
Electric Parameters	Equivalent Inductor *Lx (Lx=Me/η^2)*	0.075 H
	Equivalent Capacitor *Cx(Cx=η^2/Ke)*	3.81 x10^{-4} pF
	Equivalent Resistor *Rx (Rx=Ce/η^2)*	2.16 kohm

It is interesting to know that the lumped mass M_e of the 2D disk resonator is about 47.5% of the total disk mass, this is comparable to that of an extensional 1-D beam resonator, whose modal mass is 50% of the total beam mass. It is known that the higher percentage of equivalent lumped mass, the more efficient of a resonator structure involving in the vibration. Most importantly, the motional resistance R_x of the disk resonator is significant lower than the beam type resonator design, and the transduction coefficient η – the most important parameter of an electromechanical resonator – is more than doubled that of the correspondent extensional beam resonator [17]. High η value means high electromechanical coupling effect and it eventually translate to a low motional resistance *Rx* ($Rx=Ce/\eta^2$). The above FEA

simulation results prove that this 2D in-plane resonator design works well as expected and it has much better performance over the extensional beam resonator. In Chapter 5, the experimental measurements on the prototypes will further validate these theoretical and FEA predictions.

Chapter 3 : Fabrication Process

3.1 Introduction

The piezoelectric resonators in this study are based on heterostructure $Al_xGa_{1-x}As$ single crystal films. III-V materials are widely used for the production of high-speed VLSI circuits and laser based optical communication systems for a long time. Recently, there has been growing interest in the applications of III-V materials to the MEMS devices. In this chapter, a general overview of III-V MEMS technology is given in first section. The advantages of the $Al_xGa_{1-x}As$ family crystals are highlighted, which are the reasons behind the choice of utilizing $Al_xGa_{1-x}As$ in the RF MEMS resonators and filters. In the following section, the top-down MEMS fabrication process developed in this project is detailed. This unique process accommodates several salient features in the novel 2D contour mode resonator devised in this project such as the electrically isolated ohmic contact pads, a free standing velocity profiled resonator plate with long support beams. The fabrication process flow is described and vividly illustrated with the colored cross-section views in the last section. The hands-on work to develop the above mentioned fabrication process is conducted by another member of our team – Dr. Kumar Parshant [16]. My personal contributions to this area are mainly on the device design, mask layouts, and provide the feedbacks, comments on how to realize the 2-D resonator with good electric access and minimum parasitic impedance.

3.2 Fabrication Techniques

III-V materials are the compounds consisting of group-III element such as B, Al, Ga, In and group-V elements such as N, P, As, Sb. Due to the inherent large band gap and high mobility of electrons in these materials, they are widely used in the production of high-speed VLSI electronics, monolithic microwave IC, and laser based optical systems. GaAs is the most well-known and commonly used III-V materials in semiconductor industry. It also has other unique properties such as piezoelectric properties that are comparable to those of quartz, piezoresistive characteristics with piezoresistive values higher than those of Si, and piezooptic [18, 26]. To exploit these wonderful properties of III-V materials, more research efforts have been made recently to develop a variety of MEMS devices by using III-V materials [21, 26, 27]. An important III-V material that has been the focus of several studies for piezoelectric MEMS is $Al_xGa_{1-x}As$, including pure GaAs and AlAs [20, 27-29].

The $Al_xGa_{1-x}As$ possesses moderate piezoelectric transduction property. The highest piezoelectric coupling coefficient happens at Al mole fraction x=1, i.e. pure AlAs, which exhibits a theoretical shear-mode piezoelectric coefficient of d_{14}=3.82pC/N [18] and this value is comparable to that of quartz crystal. However, AlAs suffers from oxidization problem. To reduce the oxidation effect, a lower Al mole fraction of x=0.3, i.e. $Al_{0.3}Ga_{0.7}As$, is chosen as the transduction material in this project. Another motivation is that an $Al_{0.3}Ga_{0.7}As$ structure can be released by selectively etching off the sacrificial layer of GaAs or $Al_{0.7}Ga_{0.3}As$ underneath it. Furthermore, the technique of epitaxially grown III-V materials is well developed. In this work, the molecular

beam epitaxial (MBE) growth is used to deposit the hetero $Al_xGa_{1-x}As$ films on a clean semi-insulating 3" (100) GaAs substrate. The piezoelectric transducers based on $Al_xGa_{1-x}As$ films offer several benefits: well-characterized and low defect density epitaxial growth processes for single crystal films; the ability to integrate lattice-matched electrodes for released resonator plate with minimal stress gradients; the potential for direct integration with high-speed electronics and optoelectronics.

Unlike previously reported piezoelectric AlGaAs microstructures [20], our process employs a Cl_2-based inductively coupled plasma reactive ion etching (ICP RIE) to pattern the 2D resonator plate as well as its support beams and contact pads. The RIE is an anisotropic, physical etching, it can precisely carve the outline of a microstructure and provide a smooth and vertical side walls. But, the etching selectivity between $Al_xGa_{1-x}As$ and GaAs is poor. Hence, the time controlled etching with endpoint detection is necessary in order to achieve the desired etching depth.

Another unique feature in this MEMS resonator is the utilization of $Al_{0.3}Ga_{0.7}As$ heterostructure, where the in situ Si doped top and bottom $Al_{0.3}Ga_{0.7}As$ layers ($Al_{0.3}Ga_{0.7}As$:Si) are served as the electrodes and the transduction $Al_{0.3}Ga_{0.7}As$ layer is sandwiched between these Si doped layers. In contrast, other piezoelectric microstructures in literatures employ amorphous metal layers (e.g.: Al, Au, or Pt) as electrodes. However, these metal layers present two problems for device operation. First, the use of multiple materials introduces stress gradients, which can lead to large curvatures and nonlinearity behaviors. Second, the interfaces between multiple layers

as well as the metal films themselves are potential sources of damping, plus it has been proven that the metallization of a microstructure leads to significant increase of thermal elastic damping [8]. In the present process, the use of the lattice-matched, AlGaAs heterostructure fundamentally eliminates the above problems.

In a RF device, high parasitic capacitance can ruin its response characteristics. When RF signal is applied to a RF resonator or filter, it will be shunted away through the low impedance of the parasitic capacitance rather than through the designated device. This is called feed-through effect. Thus, a good RF device should maintain as minimum parasitic impedance as possible. Regarding the piezoelectric RF device, since piezoelectric is a good dielectric medium, the electrode contact pads in this device may introduce a considerable parasitic capacitance. Often, this parasitic capacitance is overwhelming over the device capacitance and it presents a serious challenge to MEMS RF designers. In this work, a novel approach is developed which can effectively eliminate the parasitic capacitance from the contact pads. In this solution, an isolation trench around the top electrode contact pad is created by RIE etching through the hetero AlGaAs layers. This effectively cut off the electric connection between the bottom AlGaAs:Si layer underneath the top electrode contact pad and the electric contact pad of the device. However, the top contact pad is also disconnected from the top electrode layer of the 2D resonator plate. This is fixed by the deposition of another metallic layer which bridges the top contact pad and the device top electrode layer over the parylene filled isolation trench. Comparing to the

previously developed four-mask process which has been verified on the beam type resonator design [15], this approach requires three more masks.

The 2D resonator plate has to be freestanding and suspended by the support beams. Chemical wet isotropic etching is selected to etch off the sacrificial $Al_{0.7}Ga_{0.3}As$ layer and release the resonator structure.

The whole fabrication process starts on a prepared (100) GaAs wafer where the multiple layers of AlGaAs are already grown. From this point, the fabrication starts to work from top layer to bottom layer until the resonator structure is formed. The details of this seven-mask process are presented step by step in the following section.

3.3 Fabrication Process Flow

The top-down process starts with the wafer preparation. A 2μm thick sacrificial $Al_{0.7}Ga_{0.3}As$ layer is first grown on a (100) GaAs wafer by MBE. Then, a 3-layer $Al_{0.3}Ga_{0.7}As$ heterostructure is grown on top of the sacrificial layer, with top and bottom $Al_{0.3}Ga_{0.7}As$ layers heavily Si-doped to achieve high conductivity. These electrode layers are 0.5μm thick, and the undoped piezoelectric operation layer is 1.0μm thick. Based on the prepared wafer, a seven-mask process is used to fabricate the suspended disk and metal contact pads. A finished RF device from this process is shown in Figure 3.1.

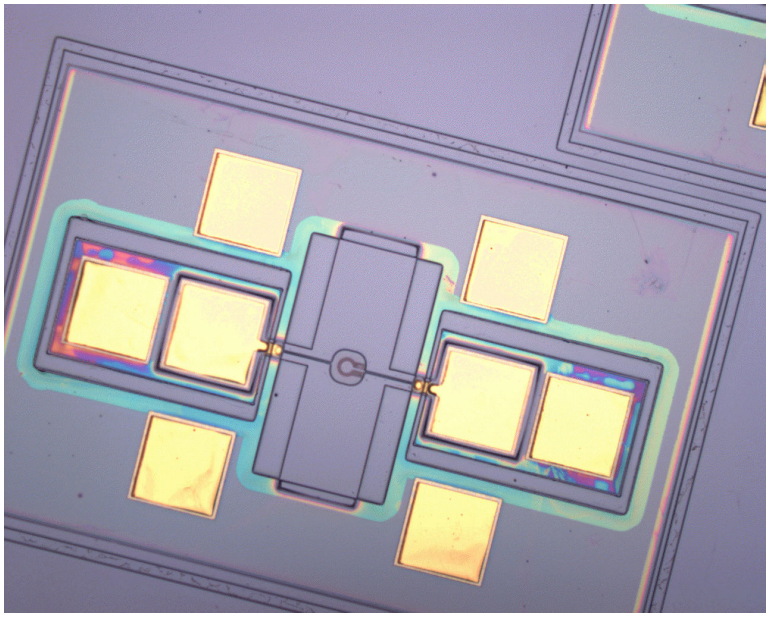

Figure 3.1: Microscopic picture of a fabricated 2D AlGaAs filter

First, a window is opened to expose the bottom $Al_{0.3}Ga_{0.7}As$ layer by ICP RIE. This opening is used to define the bottom electrode contacts. Next, metalization using a multilayer stack of Pd/Ge/Ni/Au is performed on selected top and bottom $Al_{0.3}Ga_{0.7}As$:Si electrode areas using a lift-off process, followed by rapid thermal annealing (RTA) to provide a good ohmic contact pads. In the third step, the isolation trench surround the top electrode pads is formed by ICP RIE with time controlled etching, the depth of the trench reaches the sacrificial layer. After that, the top electrode $Al_{0.3}Ga_{0.7}As$:Si layer is pattern by ICP RIE. This step is very import for the 2-port resonator design, since it defines the actuation part and sensing part electrode patterns. In the fifth step, a parylene layer is deposited on the device surface. The goal of applying this polymer conformal layer is to fill up the isolation trench and provide the support for the metal bridge which builds the electric connection between the top electric contact pad to the device top electrode. Following the parylene deposition is

the O_2-based RIE which opens a window on the metal bridge area. Then, in the eighth step, Cr/Au metal films are deposited on the whole die and the metal bridge is formed by lift-off process. After this, the remained parylene layer is etched off by RIE. In the ninth step, another mask is used to define the resonator 2D geometry, and the full $Al_{0.3}Ga_{0.7}As$ stack is etched through to the sacrificial $Al_{0.7}Ga_{0.3}As$ layer by ICP RIE. Finally, the resonator is released by etching the underlying sacrificial $Al_{0.7}Ga_{0.3}As$ film in a solution of concentrated hydrofluoric acid (HF) diluted 50% with deionized water. The HF wet etching is isotropic and provides excellent selectivity between the sacrificial $Al_{0.7}Ga_{0.3}As$ layer and structural $Al_{0.3}Ga_{0.7}As$ films. A CO_2 super critical dry is applied right after the wet etching in order to prevent the resonator plate adhering to the substrate due to capillary forces. The whole fabrication process is vividly illustrated in Figure 3.2 which shows the cross-section changes in each step of the aforementioned process.

Using this process, the 2D resonators and filters were successfully fabricated with various lateral sizes such as 100μm, 80μm, 60μm, and 40μm. While, different support beam lengths were also tried. The characterizations of these devices are presented in Chapter 5.

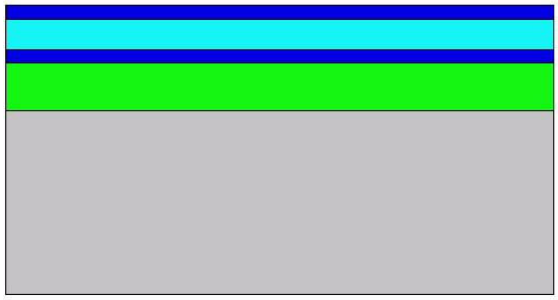

Starting wafer

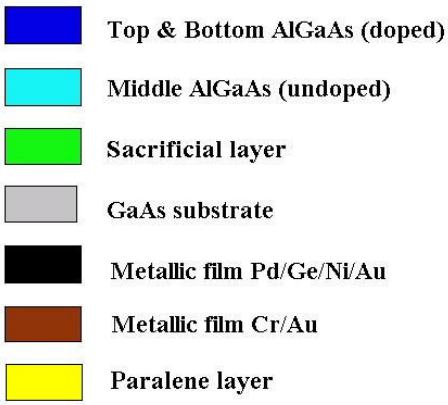

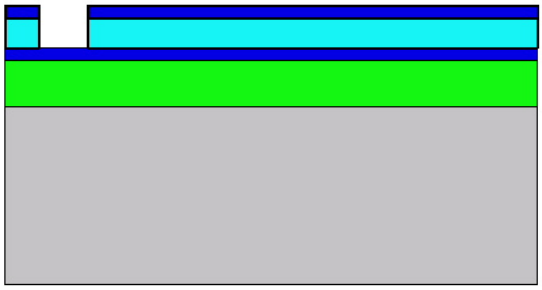

Step 1: Open window for bottom electrode contact (ICP)

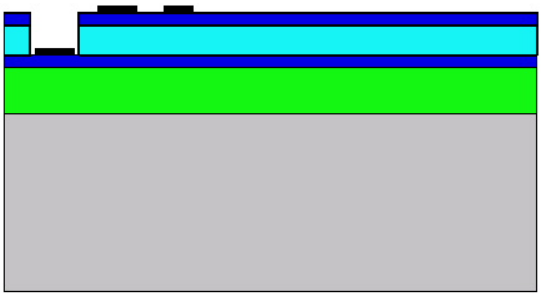

Step 2: Deposition metallic pads (ebeam evaporation)

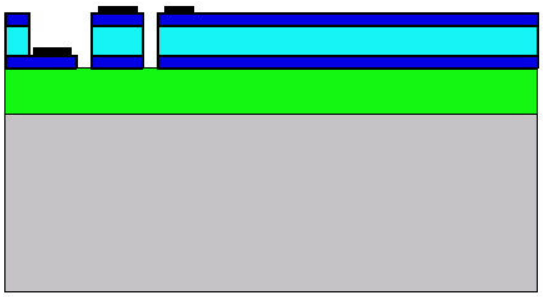

Step 3: Etch isolation trench around top contact pad (ICP)

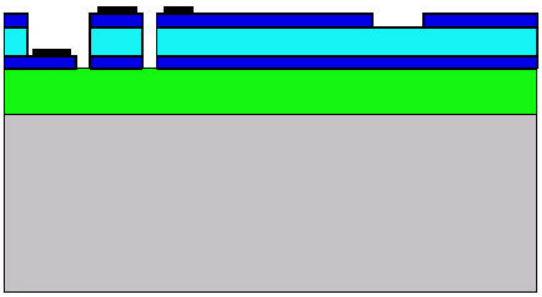

Step 4: Etch top AlGaAs layer (ICP)

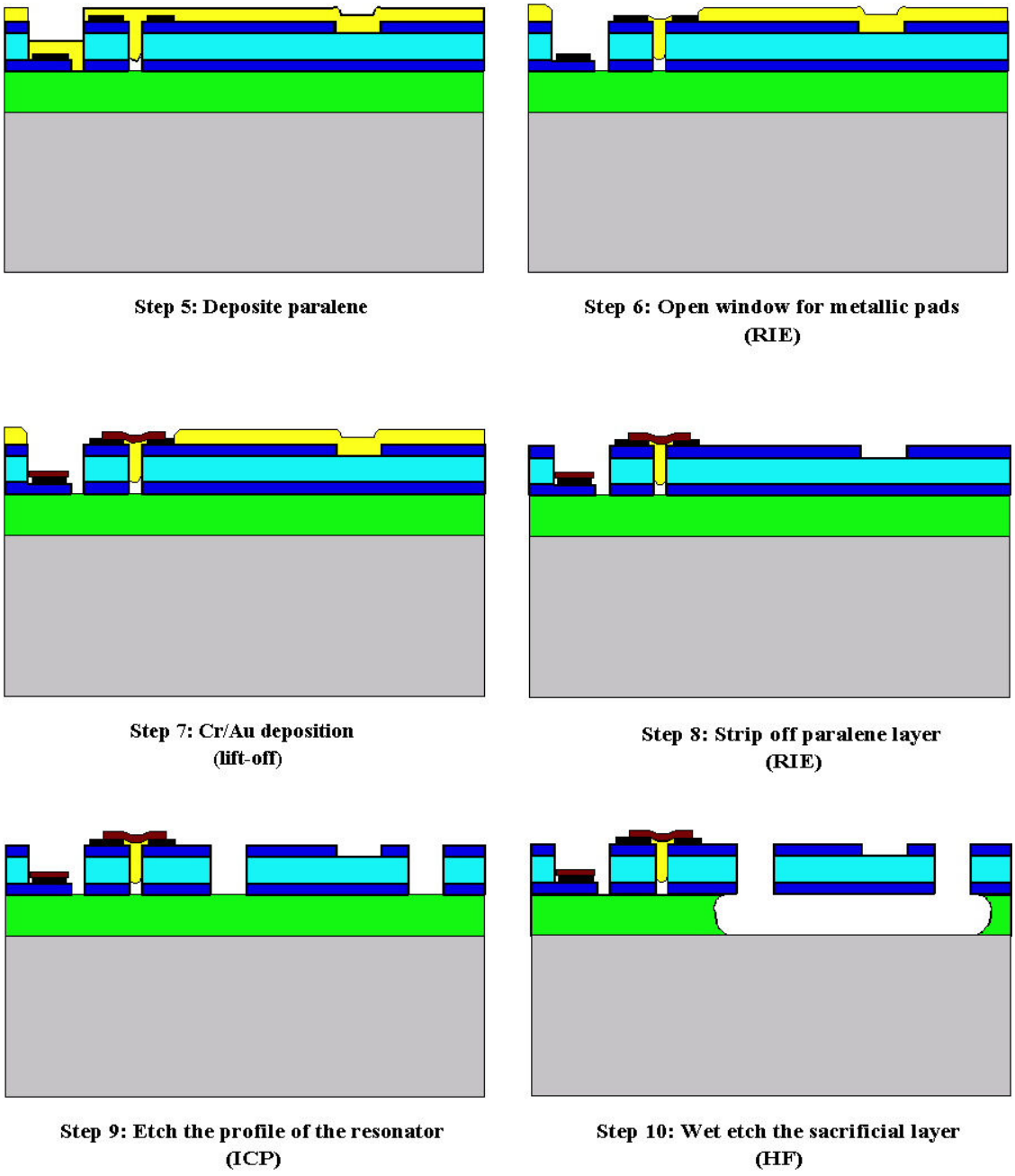

Figure 3.2: Schematics of fabrication process for AlGaAs RF devices

Chapter 4 : Energy Dissipation and Quality Factor of the AlGaAs Disk Resonator System

4.1 Introduction

It is generally desirable to have high Qs in resonators and filters for wireless communications, since the phase noise is inversely proportional to the square of Q and the insertion loss decreases as Q increases [7, 30]. The quality factor is defined as the ratio of the total energy in a resonating device to the energy dissipated within a vibration cycle; hence it is a direct indicator to the energy loss in a resonating system. In order to design a high Q resonator, it is necessary to understand what factors contribute to the energy dissipation.

The damping mechanisms in a vibrating system can be categorized into two types: extrinsic ones and intrinsic ones. Extrinsic damping usually can be minimized by proper design or change of operating conditions[31, 32]. For instance, support loss can be effectively reduced by a proper support structure design. Squeezing film damping can also be minimized by either increasing the gap between the moving plate and the substrate or employing a perforated plate instead of a solid plate. Intrinsic mechanisms, on the other hand, are more difficult to control since they depend primarily on the material and geometric properties of structures. Examples of this type are thermoelastic loss[33], surface loss[34], and bulk defect loss[35]. Thermoelastic damping is usually a dominate dissipation source in vacuum environment, especially, if a flexure vibrating mode is utilized as the operational

mode in a resonator. Intrinsic damping increases with miniaturization of devices and can be the limiting factor on the quality factors of resonators in the micro and sub-micro scales.

Considering the unique design of our 2D planar-mode plate, three energy dissipation sources are identified as the dominant factors in terms of energy dissipations, they are: anchor loss, viscous air damping, and thermoelastic damping. In this chapter, studies on these three damping mechanisms on the specific case of the 2-D resonator are carried out. Theoretical formulas for estimating the quality factors corresponding to each dissipation mechanism are presented and the total quality factor is obtained after combining all the three energy loss terms. The calculated total quality factors are compared with the measured results. This study provides us with valuable design guidance and insights to this new type resonator. Moreover, it reveals the upper limit on the quality factor for this type of resonator.

4.2 Air damping in laterally oscillating microresonators

When the microresonators are enclosed in fluid surroundings (air or other gases), the oscillating structures will excite the ambient fluid and cause energy dissipation through slide-film damping and/or squeeze-film damping. If the dimension of resonator plate is much larger than the air film thickness, the air damping will be the dominant energy dissipation source [36]. In contrast to vertically driven devices, in which squeeze-film damping is the major source of energy dissipation, viscous slide-film damping is the major dissipative source in laterally driven structures. In order to

predict the viscous fluid drag, it is necessary to accurately determine the detailed air flow around the complicated three-dimensional resonator structures. It is well known that modeling three-dimensional (3D) air damping for MEMS devices requires considerable computational resources. Based on the complicated laterally driven comb structure, several numerical methods for 3D fluid drag force prediction have been developed [37-39]. These 3D simulations involve tremendous development effort on special algorithms and code writing, in addition, the results have to be verified by experimental data. However, for a simple plate structure which vibrates laterally, 1D analytical Stokes can provide good first-order estimation on the slide-film air damping. In fact, [36, 40] have demonstrated than the 1D Couette model can predict the quality factor Q of a laterally oscillating plate very close to measured ones, about 10-20% deviation from the measured results. Since our resonator is a simple shaped 2D plate and its fundamental working mode is a planar contour mode, in our effort to estimate the viscous air damping, the 1D Stokes model for infinite sliding plate is adopted. Based on this model, the theoretical predicted Qs for different resonator sizes are obtained.

In our 2D resonator system, when the plate is oscillating laterally, a steady-state velocity profile in the ambient fluid film is formed. The fluid behavior is expected to be accurately described by solutions of the Navier-Stokes equation. For a small-amplitude motion under no overall pressure gradient, the Navier-Stokes equations reduce to[38-40]:

$$\frac{\partial v}{\partial t} = \nu \frac{\partial^2 v}{\partial z^2} \qquad (4.1)$$

where: ν is kinematic viscosity;

v is velocity distribution of fluid film.

In order to use the above equation accurately represent the fluid behavior around a moving planar structure, the following conditions have to be satisfied.

- The minimum size of the microstructure and fluid-film thicknesses would be much larger than the mean free path of gas (the mean free path of air is 0.065μm)
- The width and length of the plate are much larger than the sliding film thickness (satisfy the infinite planar assumption).
- The amplitude of the oscillation is small compare with the minimum feature size of the microstructure.

After scrutinizing our 2D resonator design, we are sure that all the above conditions are satisfied.

Equation (4.1) is solved in the frequency domain for a steady-state sinusoidal velocity excitation with amplitude of u_o and angular frequency ω_o. The solution can be written in the form

$$v(z) = C_1 \cdot \sinh(q \cdot z) + C_2 \cdot \cosh(q \cdot z) \qquad (4.2)$$

where: $q = \sqrt{j\omega_o / \nu}$ is the complex frequency variable;

constant C_1 and C_2 are determined from the boundary conditions.

The boundary conditions for the fluid flow above the plate are: at plate v(0) = u_o; far away from the plate v(∞) = 0. Combine with the above solution, the velocity function of the fluid above the plate is determined.

$$v(z) = u_o \cdot e^{-q \cdot z} \tag{4.3}$$

where: u_o is the oscillating amplitude of the plate.

The boundary conditions for the fluid flow beneath the plate are: at the substrate v(-d) = 0; near the oscillating plate v(0) = u_o. The velocity function is obtained,

$$v(z) = u_o \cdot \frac{\sinh(q \cdot (d + z))}{\sinh(q \cdot d)} \tag{4.4}$$

The derived fluid velocity solutions and the associated coordinate system and the vibrating plate are explicitly illustrated in Figure 1.

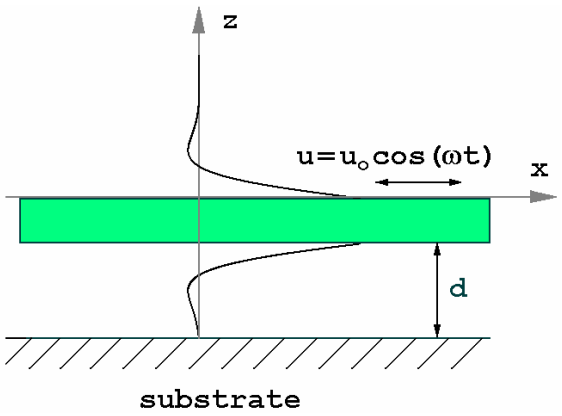

Figure 4.1: Velocity profiles of fluid layers induced by a laterally oscillating plate

According to the Newton's law of viscosity[40], the drag shear stress, τ_o, on the plate surface is proportional to the velocity gradient at the surface:

$$\tau_o = \mu \frac{dv}{dz} \tag{4.5}$$

Due to the friction shear stress τ_o, the fluid-film acts as a dashpot and it dissipates the amount of energy D in one cycle,

$$D = \frac{1}{\omega} \cdot \int_0^{2\pi} \tau_0(\omega t) \cdot v(\omega t) d(\omega t) \tag{4.6}$$

The Q factor of a resonator system is defined as the ratio of the total energy stored in the resonator system, W, to the energy dissipated through the plate area, A:

$$Q = \frac{2\pi \cdot W}{A \cdot D} \tag{4.7}$$

Our 2D plate microresonator can be modeled as a lumped parameter system which consists of mass M, spring K, and dashpot C. Based on this single-degree-of-freedom (SDOF) lumped model, the quality factors due to the top viscous fluid damping Q_{top} and bottom viscous fluid damping Q_{bottom} can be derived from equation (4.7).

$$\begin{aligned} Q_{top} &= \frac{\sqrt{M \cdot K}}{\mu \cdot \beta \cdot A} \\ Q_{bottom} &= \frac{\sqrt{M \cdot K}}{\mu \cdot \beta \cdot A} \cdot \frac{(\cosh(2\beta d) - \cos(2\beta d))}{(\sinh(2\beta d) - \sin(2\beta d))} \end{aligned} \tag{4.8}$$

where: $\beta = \sqrt{\omega_o / 2v}$;

μ is the absolute viscosity of the ambient fluid.

In our case the microresonator is exposed to atmosphere, therefore the ambient fluid is air. The overall Q_{air} factor due to air slide-film damping is estimated as:

$$\frac{1}{Q_{air}} = \frac{1}{Q_{top}} + \frac{1}{Q_{bottom}} + \frac{1}{Q_{end}} \tag{4.9}$$

where: Q_{end} is the quality factor from the end surface effect.

If the oscillating plate is infinite large or the ratio of the lateral dimension to the thickness is much larger, then the end air damping effect is not significant and the Q_{end} can be neglected. But, if a resonator has comparable lateral dimensions relative to its thickness, the end air damping effect will play an important role in the overall damping. For large plates, this term is usually ignored from equation (4.9). This results in the quality factor Q_{air} obtained from the Stoke sliding film model is usually overestimated. In fact, it is believed that the 10-20% deviations between the calculated quality factor Q_{air} and the measured air damping quality factor in[36, 40] is due to this end effect.

Applying equation (4.8) and using the FEA model determined mass M and spring K, the quality factor Q_{air} of our 2D resonator is obtained. Table 1 lists the calculated Q_{air}s correspondent to different plate sizes. Keep in mind that these calculations exclude the end air damping effect, as the plate size becomes smaller, the estimated Q_{air} may be more optimistic.

Table 4.1: Estimated Q_{air} factors based on the Stoke sliding film model

Resonator Lateral Size	100μm	80μm	60μm	40μm
Q_{air}	18,165	20,378	23,684	29,384

4.3 Anchor loss (a.k.a. support loss) through support beams

Ideally, the 2D, planar, AlGaAs piezoelectric resonator should be freely suspended in air. But, to keep it in a fixed position in space, it has to be supported and attached to the frame of the substrate. In the current design, it is supported by slender beams, as shown in Figure 4.2; one end of the beam is located at the resonator's nodal points at the middle of the plate, and the other end is fixed with the structural frame. This support structure can be modeled as a clamped – pined beam (C-P), and it is depicted in Figure 4.3. There are two major energy dissipation sources in this supporting system: one is the anchor loss at the clamped end; the other is the thermoelastic loss within the beam.

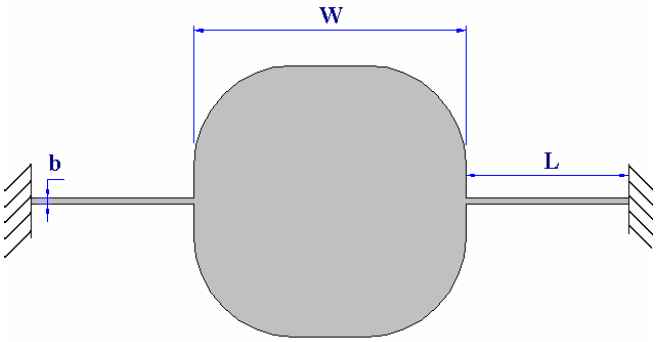

Figure 4.2: 2D AlGaAs resonator with two support beams

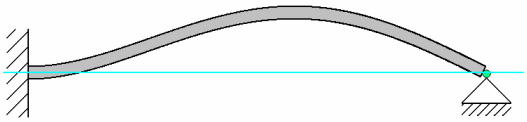

Figure 4.3: Support beam model: clamped-pined (C-P) beam

Support loss, also called as anchor loss, is the vibration energy of a resonating object dissipated by transmitting a portion of this energy into the supporting substrate. During the in-plane vibration, the support beam exerts both dynamic shear force and

moment at the clamped end. Figure 4.4 illustrates the shear stress τ_n and normal stress σ_n induced by the beam to the elastic base.

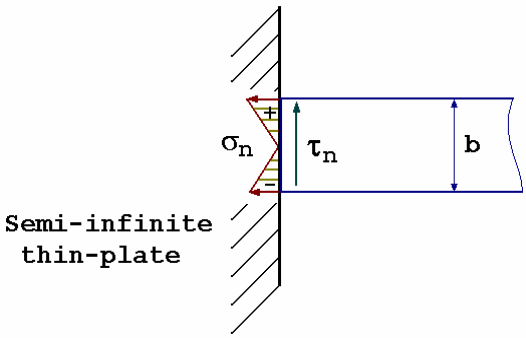

Figure 4.4: Excitation source from an in-plane bending beam to a semi-infinite plate

The perturbation force will excite elastic waves, which propagates into the infinite elastic base without reflection and is considered as the anchor loss of this system. In most cases, the elastic wavelength is much larger than the thickness and width of the beam. Under this condition, the support loss due to the moment (generated by normal stress σ_n in Figure 4.4) has been proved to be negligible compared to that incurred by the vibrating shear force [41, 42]. In our 2D resonator system, this assumption is satisfied. For instance, for a lateral size 80μm 2D resonator, its wavelength is equal to the double of the plate size, i.e. 2x80μm, which is much larger than the support beam cross-section dimensions (≤5μm).

Z. Hao [41] and M.C. Cross [42] have laid the foundation of the analytical framework for a vibrating beam attached to a semi-infinite plate and both have the same thickness. In their work, the shear force at the end of the beam and the plate displacement at the anchor location induced by the shear stress are analytically

derived. And, the work done by the shear force is calculated and treated as the anchor loss. In our resonator design as illustrated in Figure 4.2, the support beam is located at the nodal point of the 2D plate, so the beam can be modeled as a C-P beam. In addition, if one considers the undercut at the frame plate created by the releasing wet-etch process, then the analytical 2D model defined in [41, 42] is a good representation to our beam support system. In this study, we employ the solutions from [41] to our support beam and determine its quality factor Q_{ban} due to the anchor loss.

To determine the anchor loss at the end of the beam, the resonating mode shape has to be known. For a C-P beam, it has the mode shape function Φ(x) [43],

$$\phi_i(x) = A_i \cdot \left[\cosh(\lambda_i \cdot \frac{x}{L}) - \cos(\lambda_i \cdot \frac{x}{L}) + \chi_i \cdot (\sinh(\lambda_i \cdot \frac{x}{L}) - \sin(\lambda_i \cdot \frac{x}{L})) \right] \tag{4.10}$$

where: λ_i is the eigenvalue of the characteristic equation: $\tanh(\lambda) \cdot \cot(\lambda) = 0$;

χ_i is the mode shape factor and is expressed as $\chi_i = -\frac{\cosh(\lambda_i) - \cos(\lambda_i)}{\sinh(\lambda_i) - \sin(\lambda_i)}$;

subscript i denotes different resonant mode numbers (i = 1,2,3, …).

Table 4.2 gives the first 10 mode shape factors and the correspondent roots of a C-P beam.

Table 4.2: Mode shape factor χ and the correspondent eigenvalue λ for a C-P beam

Mode	1	2	3	4	5	6	7	8	9	10
λ	3.92	7.07	10.21	13.35	16.49	19.64	22.78	25.92	29.06	32.20
χ	-1	-1	-1	-1	-1	-1	-1	-1	-1	-1

The quality factor Q_{ban} for a C-P beam, when only the anchor loss is taken into account, is given as,

$$Q_{ban} = \left[\frac{0.239 \cdot (1-\nu)}{\psi \cdot (1+\nu)}\right] \frac{\pi^2}{(\lambda_i \cdot \chi_i)^2} \left[\frac{L}{b}\right]^3 \tag{4.11}$$

where: L is beam length;

b is beam width;

υ is Poisson's ratio;

Ψ transmission coefficient and is given as,

$$\psi = \int_0^\infty \frac{\sqrt{\varsigma^2 - (v_l / v_t)^2}}{\left[2\varsigma^2 - (v_l / v_t)^2\right]^2 - 4\varsigma^2 \cdot \sqrt{\varsigma^2 - (v_l / v_t)^2} \cdot \sqrt{\varsigma^2 - 1}} d\varsigma \tag{4.12}$$

where: v_l is longitudinal elastic wave speed;

v_t transverse elastic wave speed.

The imaginary part of the integral contributes to the support loss and it can be calculated numerically. The Q_{ban} equation (4.12) shows that the anchor loss is proportional to the cube of (b/L), which implies that the longer and narrower beam, the smaller its anchor loss. This conclusion agrees with the design practice for support structure of bulk resonators. Often, the bulk resonator is suspended by means of a very-low-impedance support such as long, compliant strings [44].

In our microresonator experiments, two types of support beams are implemented: one has the width 5μm with various beam lengths; the other is 2μm with a variety of lengths.

The single crystal $Al_{0.3}Ga_{0.7}As$ beam is along <001> direction, thus, it has the following material properties: $\upsilon = 0.315$, $v_l = 4943$ m/sec, $v_t = 3484$ m/sec, $E = 84.68$ GPa. And, from equation (4.10), the Ψ is numerically calculated, $\Psi = 0.504$.

Now one can apply the theoretical solution of equation (4.11) to solve the quality factor Q_{ban} for each type of the beam. Tabel 4.3 and Table 4.4 summarize all the Q_{ban}s from these calculations.

Table 4.3: Anchor loss quality factor Q_{ban} for support beam width b = 5 μm

Resonator Size W	100 μm			80 μm			60 μm
Beam Length L	110 μm	130 μm	150 μm	50 μm	90 μm	130 μm	30 μm
Quality Factor Q_{ban}	*81.3*	*111.0*	*126.8*	*23.4*	*52.2*	*82.5*	*10.5*

Table 4.4: Anchor loss quality factor Q_{ban} for support beam width b = 2 μm

Resonator Size W	80 μm		60 μm		40 μm	
Beam Length L	48 μm	5 μm	61 μm	41 μm	38 μm	5 μm
Quality Factor Q_{ban}	*188.9*	*2.5*	*179.2*	*117.7*	*61.4*	*2.5*

Please note that the hereby quality factor Q_{ban} is for the support beam only, not for the whole 2D resonating system. Actually, in the last section of this chapter, we will deal with the translation of these Q factors into the whole resonator system ones.

4.4 Thermoelastic damping of the support beam

In vacuum, thermoelastic (TE) damping has been shown to be a major source of energy dissipation in microresonators. In a thermoelastic solid, the strain field is coupled to a temperature field; compression stress increased temperature and tension stress lower temperature. Therefore, an oscillating stress gradient generates a correspondent temperature gradient. The irreversible heat flow due to the temperature gradient in the thermoelastic solid results in the energy dissipation, i.e. TE damping [8, 32, 33]. This TE damping presents an upper limit to the quality factor of an even the most perfectly designed and constructed resonator.

For a flexural vibration beam, the compression and tension stresses happen on the top and bottom surfaces of the beam. Hence, the temperature gradient is defined by the beam thickness. In contrast, a longitudinal mode vibration plate, which is the case of the most in-plane vibration modes, the temperature gradient is defined by the wavelength instead. In most cases, the acoustic wavelength is much larger than a beam thickness, hence, a flexural mode beam suffers much more TE dissipation than a longitudinal mode object [45].

Thermoelastic damping is governed by the dynamic equilibrium and heat conduction partial differential equations[46]:

$$\frac{E}{2(1+\nu)(1-2\nu)} \cdot \frac{\partial e}{\partial x_i} + \frac{E}{2(1+\nu)} \cdot \nabla^2 u_i - \rho \ddot{u}_i = \frac{E\alpha}{(1-2\nu)} \cdot \frac{\partial T}{\partial x_i} \tag{4.13}$$

$$k \cdot \nabla^2 T - C \cdot \frac{\partial T}{\partial x_i} = \frac{E\alpha T_0}{(1-2\nu)} \cdot \frac{\partial e}{\partial x_i} \tag{4.14}$$

where: α is the linear thermal expansion coefficient;

E is Young's modulus;

ν is Poisson ratio;

k is the thermal conductivity;

ρ is the material density;

C is the thermal capacity per unit mass;

T_0 is the equilibrium temperature;

$e = \varepsilon_{11}+\varepsilon_{22}+\varepsilon_{33,}$ the volume dilatation;

i = 1,2,3.

Clearly, the mechanical field is coupled with the temperature field in equation (4.13) and (4.14).

If a vibration mode has no volume change at any local places (e = 0) in the object, then theoretically, this vibrating object suffers no TE losses [33]. It is known that shear deformation causes no volume change; therefore, any oscillators operating in pure shear (or. torsion) modes suffer no TE damping. For example, a pure torsion mode of a beam involves no local volume changes. Hence, it does not have any thermoelastic losses when vibrating at this mode.

Regarding our MEMS resonator design, shown in Figure 4.2, since the 2D AlGaAs plate resonates at the in-plane longitudinal mode and the support beam vibrates at the flexural mode, the TE energy dissipation will mostly happen in the support beams. Moreover, since the shear stress is dominant in the resonating planar contour mode; the TE energy loss has minimum effect in the 2D resonator. However, in practice the in-plane vibrating mode inevitably induce some flexural component due to the non-perfect symmetry of the structure. So, the TE dissipation exists even in a nominal shear vibration mode. Since the TE damping induced by the parasitic flexural modes is hard to be determined analytically, it has to be characterized through experiments [47].

In the following, we will apply the theoretical solution of TE damping for a homogeneous beam in flexural modes developed in [33] to the support beams in our resonating system and calculate the quality factor of the beam due to the TE damping. The support beam is made from epitaxial layer of $Al_{0.3}Ga_{0.7}As$ crystal, and it can be treated as a homogeneous beam.

The dimensionless Zener modulus Ψo is defined as [8]: $$\Psi_0 = \frac{2\pi \cdot E\alpha^2 T_0}{\rho C} \quad (4.15)$$

From the material perspective, Zener modulus is a good indicator about the thermoelastic damping phenomenon in a material. It is true that under the same conditions, the larger the Zener modulus is, the severer thermoelastic damping will be.

Table 4.5 lists the thermal, elastic properties of most common materials used in MEMS structures.

Table 4.5: Nomial material properties at 300K [8, 18]

Crystal Formula	E (GPa)	ρ (kg/m^3)	$\sqrt{E/\rho}$ (m/sec)	k (W/m/K)	C (J/kg/K)	α (10^{-6}/K)	Ψo Zener Modulus
GaAs	85.3	5360	3989	44	334.9	6.4	0.0037
$Al_{0.3}Ga_{0.7}As$	84.8	4880	4168	12	372.6	6.0	0.0032
Si	160	2330	8287	150	686.7	2.6	0.0013
Si_3N_4	250	3200	8839	8	937.5	3.0	0.0014
Quartz SiO_2	70	2200	5641	1.2	681.8	0.5	0.00002

From Table 4.5, it is clear that the quartz crystal has the best performance in terms of TE damping. That explains why most of bulk, discrete resonators have accepted this material. In the MEMS world, GaAs has moderate Zener modulus, and $Al_{0.3}Ga_{0.7}As$ has slightly better Zener modulus than that of GaAs crystal. The TE damping in the support beams can be approximated by Zener's formula [46]

$$\Psi = \Psi_0 \cdot \frac{\Omega}{1+\Omega^2} \tag{4.16}$$

where: Ψ is the magnitude of thermoelastic damping;

Ω is the dimensionless frequency and is defined as, $\Omega = \omega \cdot \tau = \omega \cdot \frac{b^2 \rho C}{\pi^2 k}$

(4.17)

where: ω is the angular frequency;

τ is the time constant associated with thermal diffusion;

b is the beam thickness;

Based on the equation (4.17), it is not hard to prove that the thermoelastic damping Ψ reaches a maximum value Ψo/2 when the normalize frequency Ω equals 1. The function of Ψ(Ω) is plotted in Figure 4.5.

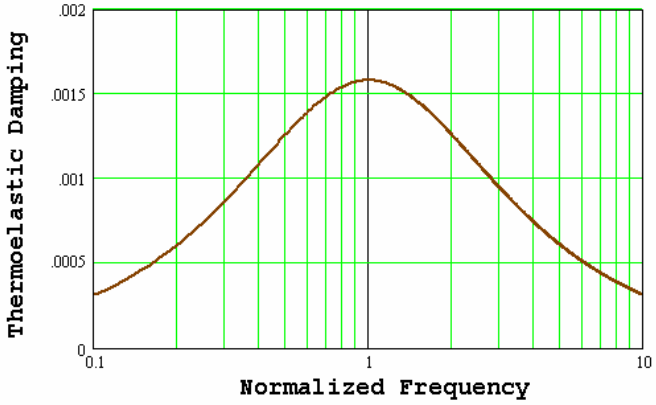

Figure 4.5: Frequency dependence of thermoelastic damping in $Al_{0.3}Ga_{0.7}As$ beam

For a beam width b=2μm, the Ω = 1 condition corresponds to a vibration frequency $f_{TE} = 1/(2\pi\tau) = 2.59$ MHz. When design a resonator, one has to avoid this frequency in order to minimize the thermoelastic damping. Fortunately, all our 2D resonators vibrate at much higher frequency than f_{TE} (Ω >>1).

For the support beam shown in Figure 4.3, the quality factor Q_{bTE} of the beam due to its thermoelastic damping can be simply calculated from equation (4.16) as,

$$Q_{bTE} = \frac{1}{\Psi} \qquad (4.18)$$

Table 4.6 list the quality factor Q_{bTE} for all the support beams in this study.

Table 4.6: Quality factor Q_{bTE} of thermal elastic damping

Resonator Size W	100 μm	80 μm	60 μm	40 μm
Beam Width b = 5 μm	18,053	22,864	30,834	47,151
Beam Width b = 2 μm	2,921	3,684	4,953	7,557

Note that the TE damping in a flexural bending mode beam is independent to the beam length as well as its vibration modes. Comparing the Q_{TE} to the other Qs obtained in previous section, since $Q_{bTE} >> Q_{ban}$, it is evident that the anchor loss and viscous air drag is the dominant energy dissipation source in this oscillating system.

4.5 Overall quality factor of the resonator system

The above quality factor calculations, the Q factors derived from the anchor loss and TE dissipation are for the support beams only, they are not the Q factors for the whole 2D resonating system. In this section, we first convert the Q factors of the support beam into the ones for the whole resonator. Then, we combine all the Q factors derived from different energy dissipation mechanisms to form the overall quality factor Q of the resonator system.

In our 2D resonator, the total energy W_{total} is comprised by two parts: the support beam energy and the 2D resonator energy. From the FEA models created in ANSYS10.0, the mechanical potential energy ratios of the resonator plate to the support beams for different designs are retrieved. For example, when an 80 μm 2D resonator with dual 48 μm support beams resonating at its operational mode, the FEA

model tells that the energy ratio $W_{total}/ W_{beam} = 495$. Figure 4.6 illustrates the resonant mode shape obtained from the FEA simulation.

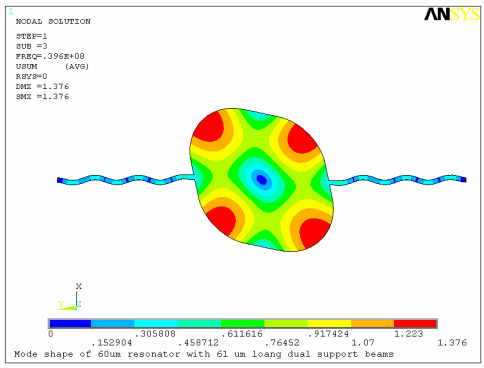

Figure 4.6: The colored contour of mode shape obtained from FEA

Once the energy ratio is known, one can simply convert the beam level quality factor into the whole system quality factor by multiplying it with this ratio such as: $Q_{an} = 495Q_{ban} = 93{,}543$; $Q_{TE} = 495Q_{bTE} = 1{,}762{,}200$, where Q_{an} and Q_{TE} are the system level quality factors due to the anchor loss and TE damping in the support beams.

According to the definition of the quality factor Q of a resonating system,

$$Q = 2\pi \frac{W_{total}}{\Delta W} \tag{4.19}$$

where: ΔW denotes the energy dissipated per cycle of vibration;

W_{total} is the total energy of the resonating system.

In the above study, each energy dissipation source is treated separately. Since, these energy dissipation sources are independent to each other, one can simply sum all the energy loss terms to obtain the total energy loss ΔW as, $\Delta W = \sum \Delta W_i$, where ΔW_i represents the energy loss from each different dissipation mechanism. Based on this

relation, the total quality factor Q can be calculated d by the individual quality factor Q_i,

$$\frac{1}{Q} = \sum_i \frac{1}{Q_i} \qquad (4.20)$$

After applying equation (4.20), the total quality factor Q of the resonator system is then determined. Table 4.7 and 4.8 summarize the overall quality factors for all the cases that we fabricated and tested.

Table 4.7: Q factors of the 2D resonators with support beam width b = 5 μm

Resonator Size W	100 μm			80 μm			60 μm
Beam Length L	110 μm	130 μm	150 μm	50 μm	90 μm	130 μm	30 μm
Quality Factor Q_{air}	18,165			20,378			23,684
Quality Factor Q_{an}	13,608	16,632	26,628	7,287	9,031	10,725	8,361
Quality Factor Q_{TE}	3.65M	3.64M	3.61M	7.12M	3.96M	2.97M	25.20M
Quality Factor Q	**7,763**	**8,662**	**10,766**	**5,364**	**6,248**	**7,010**	**6,178**

Table 4.8: Q factors of the 2D resonators with support beam width b = 2 μm

Resonator Size W	80 μm		60 μm	40 μm	
Beam Length L	48 μm	5 μm	41 μm	38 μm	5 μm
Quality Factor Q_{air}	20,378		23,684	29,384	
Quality Factor Q_{an}	95,343	4,713	*28,460*	56,304	5,269
Quality Factor Q_{TE}	1.82M	41.05M	1.20M	6.93M	15.93M
Quality Factor Q	**16,636**	**3,824**	**12,789**	**19,254**	**4,467**

The above quality factor calculations are based on the first-order theoretical models from three major energy dissipation sources, apparently, the other secondary energy loss mechanisms, such as surface loss, radius corners induced TE and anchor loss, are not considered. However, these estimated Q factors given in Table 4.7 and 4.8 still reveal much information about how the geometries of this resonator will affect its overall Q factor, and also bring out insights to this unique resonator system. Several interesting points can be drawn from these results.

Among the three damping mechanisms, the thermal elastic damping in the flexural bending support beams have the least effect to the overall quality factor Q of the 2D resonator system. Since the Quality factor from the TE damping are more than two orders of magnitude larger than the Q factors from anchor loss and air fluid damping. However, as [47] point out that the flexural bending mode is inevitably induced during oscillating due to non-perfect symmetry of the resonator plate, and the non ideal shear stress state around the beam joint area, in real world the TE damping could be much larger (2-3 times) than the ones calculated from the ideal shear mode conditions. But these additional TE damping effects are hardly predicted by theoretical models and they are usually determined by empirical measurements.

In the case of short support beams, the anchor loss is the dominant loss mechanism and the support loss determines the upper limit on Q. If one can effectively reduce the anchor loss, then the quality factor of the system will be greatly improved. In this situation, placing the resonators in vacuum would not help to increase the Q factors.

As for the cases of long support beams, the air damping starts to play an important role in the overall Q factor. In this planar, contour mode 2D resonator, the air damping mostly comes from the sliding-film viscous friction, which has much less damping effect than the squeezing-film air damping in the out-of-plate resonators. As mentioned before, the end effect of air damping is not counted here, as the lateral size of the resonator plate become smaller; this end effect contributes more portions to the overall air damping.

In general, the predicted quality factors are promising, and they are an order of magnitude higher than that of the beam type counterparts [48]. In the following chapter, the real Q factors of the prototypes are measured both in atmosphere and in vacuum. Measured Qs are compared with the estimated Qs given in Table 4.7 and 4.8, demonstrating the same trends as observed in the theoretical predictions.

Chapter 5 : Performance Characterization and Verification

5.1 Introduction

Regarding the application of resonator, the parameters of major interest are resonance frequency f_r, motional resistance R_x, quality factor Q, dynamic range (power handling capability), and thermal stability. In this study, the AlGaAs disk resonators are characterized in all the five aspects. A variety of AlGaAs disk resonators, whose resonance frequencies range from 24 MHz to 62 MHz, with different support beam lengths are fabricated and characterized. The prototypes are made in two batches in this study. The first batch uses the contact film masks which have low cost, buy relative low resolution. It has the thickness 0.5μm/4μm/0.5μm correspondent to the heterostructure of $Al_{0.3}Ga_{0.7}As$:Si, $Al_{0.3}Ga_{0.7}As$, $Al_{0.3}Ga_{0.7}As$:Si multi-layers; four support beam with 5μm width are implemented and they are located at the nodal points of the disk. The second batch uses project masks which cost more but have higher resolution. The thicknesses of the $Al_{0.3}Ga_{0.7}As$ heterostructure are 0.5μm/1μm/0.5μm; dual support beams with 2μm width are employed in this case. The scaled schematic view of the fabricated prototypes is shown in Figure 5.1. The experimental results are compared with the analytical and numerical simulation results. Brief discussions on the tested results are given.

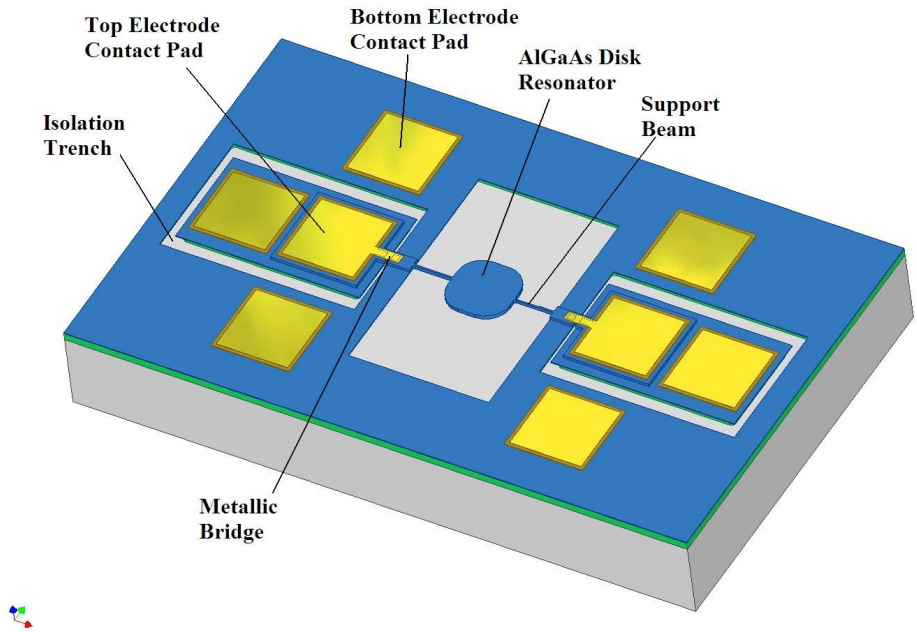

Figure 5.1: Perspective view of the single port AlGaAs disk resonator

5.2 Motional resistance measurement

The equivalent circuit model of a single-port piezoelectric resonator may be represented by the classical Butterworth-Van Dyke model shown in Figure 2.12. At resonance, the overall resonator impedance is equivalent to the motional resistance R_x in parallel with the piezoelectric static capacitance C_o. The motional resistance R_x dominates, since the capacitive impedance due to C_o is much larger than R_x at resonance. Motional resistance is a critical resonator parameter, with impedance matching to 50 Ω RF electronics generally desired. Motional resistance for the fabricated resonators was measured using a transmission/reflection test set (HP 87512A) connected to a network analyzer (HP 4395A), with the resonators directly connected to the 50 Ω input and output ports of the network analyzer. Values for

motional resistance were determined through the measurement of insertion loss at resonance (IL), and applying the following relationship [5]:

$$R_x = 50\Omega \cdot (10^{\frac{IL}{20}} - 1) - R_P \qquad (5.1)$$

In this equation, R_p is the total parasitic resistance in series with the device under test, which must be subtracted from the total measured resistance to determine the intrinsic value of R_x. For our resonators, the parasitic impedance is primarily defined by the resistance of the $Al_{0.3}Ga_{0.7}As$:Si electrodes connecting the bond pads with the resonator through the support beam. Using a measured value of resistivity for the silicon-doped $Al_{0.3}Ga_{0.7}As$ electrodes of 0.002 Ω cm, together with the known electrode geometries, R_p is estimated. In this measurement, the resonance frequency of the device is also identified. Figure 5.2 presents a typical frequency response of a 40 μm disk resonator obtained from this measurement.

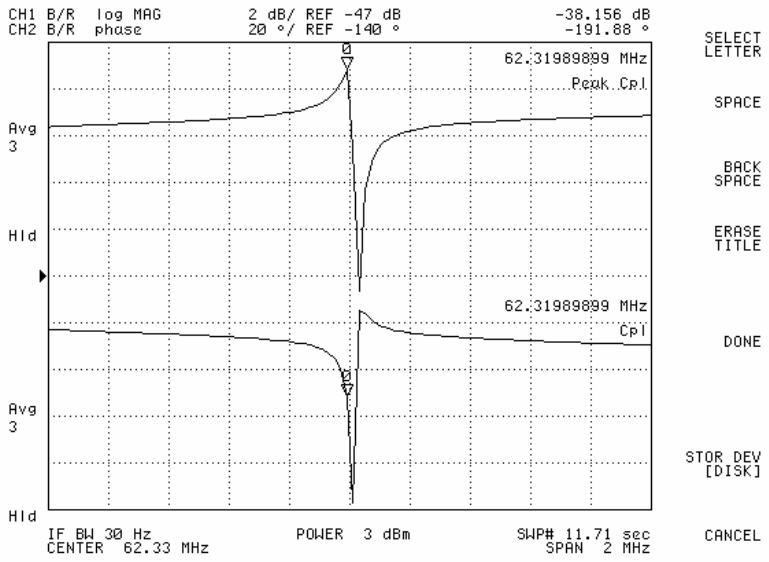

Figure 5.2: Transmission response of 40 μm $Al_{0.3}Ga_{0.7}As$ disk resonator

There are two batches of the prototypes have been fabricated and both of them were fully evaluated. The difference between these two batches of the AlGaAs disk resonators are summarized in Table 5.1.

Table 5.1: The differences between the two batches of the prototypes

	Number of support beams	Beam width	Thickness of hetero-AlGaAs films
Batch 1	4	5 μm	0.5/4.0/0.5 μm
Batch 2	2	2 μm	0.5/1.0/0.5 μm

The measured values of f_r, and R_x are summarized in Table 5.2 and 5.3, together with the analytical and finite element predictions for resonance frequency. Moreover, the intrinsic motional resistances of the AlGaAs disk resonators are extracted by subtracting the support beam impedance R_p from the total measured impedance and they are listed in Table 5.2 and 5.3.

Table 5.2: Transmission test results from the prototypes of the first batch

		60 μm disk	80 μm disk	100 μm disk
Resonance frequency	modeled (FEM)	39.7 MHz	29.8 MHz	23.8 MHz
	modeled (analytic)	41.2 MHz	30.8 MHz	24.7 MHz
	Experimental f_r	38.1 MHz	29.0 MHz	23.3 MHz
Measured total impedance (R_p+R_x)		3.62 kΩ	4.40 kΩ	4.50 kΩ
Minimum motional resistance R_x		3.09 kΩ	2.22 kΩ	1.67 kΩ

Table 5.3: Transmission test results from the prototypes of the second batch

		40 μm disk	60 μm disk	80 μm disk
Resonance frequency	modeled (FEM)	59.6 MHz	39.7 MHz	29.8 MHz
	modeled (analytic)	61.0 MHz	41.2 MHz	30.8 MHz
	Experimental f_r	62.3 MHz	40.8 MHz	30.2 MHz
Measured total impedance (R_p+R_x)		3.94 kΩ	3.70 kΩ	1.31 kΩ
Minimum motional resistance R_x		2.43 kΩ	1.26 kΩ	1.11 kΩ

Overall, the motional resistances show substantial improvement, more than 4 times reduction compared to the piezoelectric extensional-mode beam resonators when operating in the same frequency range [15]. Also, we have observed that regardless the beam length, the resonant frequencies for each disk size remained virtually unchanged, with less than 0.2% variation. This indicates that the nodal-point located support beams have minimum effect on the disk resonator. When comparing the motional resistances R_x between the two batches, it is interesting to see that when the resonance is same (same disk size), the motional resistances from the first batch are more than double that of the prototypes from the second batch. As shown in Table 5.1, the first batch has 4 support beams in each resonator and the width is 5 μm, whereas only 2 support beams with the width of 2 μm are used in the second batch. Consequently, the resonators from first batch suffer much more anchor loss than the ones from second batch. High energy loss will reflect on the higher motion resistance. In general, few support beams and narrow beam width will effectively cut down the anchor loss, and eventually yield better resonator performance.

5.3 Quality factor Measurement

Fabricated chips were characterized in air on an RF-1 probe station (Cascade Microtech, Beaverton, OR), with electrical contacts made using coaxial RF probes placed on adjacent metal bond pads. The prototypes from the second batch are also measured at moderate vacuum level (100 μTorr) on an RF vacuum probe station (Desert Cryogenics TT-Prober). All the qualify factors were measured using an impedance bridge scheme [15], which is illustrated in Figure 5.3. In this bridge, the resonator acts as one branch of a capacitive bridge circuit, with the opposite defined by matched an on-chip piezoelectric capacitor defined by an identical resonator which has not been released from the substrate. The remaining two branches are defined by passive off-chip capacitors which may be tuned to balance the bridge. When fully balanced, the output voltage between the two branches is zero, but as the device impedance drops near resonance the bridge becomes unbalanced, and the resulting output voltage is fed to a differential voltage amplifier monitored using an HP 4395A network analyzer. A typical resonant response from this measurement is shown in Figure 5.4. Measured Q factors are listed in Table 5.3 and 5.4

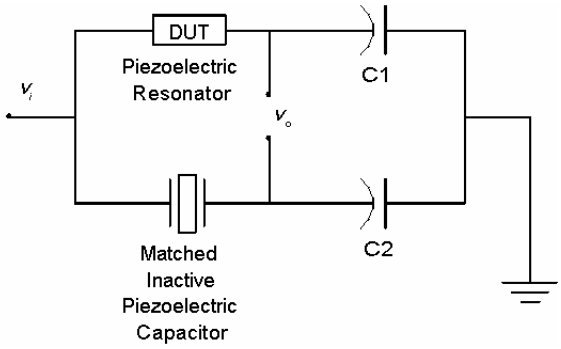

Figure 5.3: Impedance balanced bridge for Q factor measurement

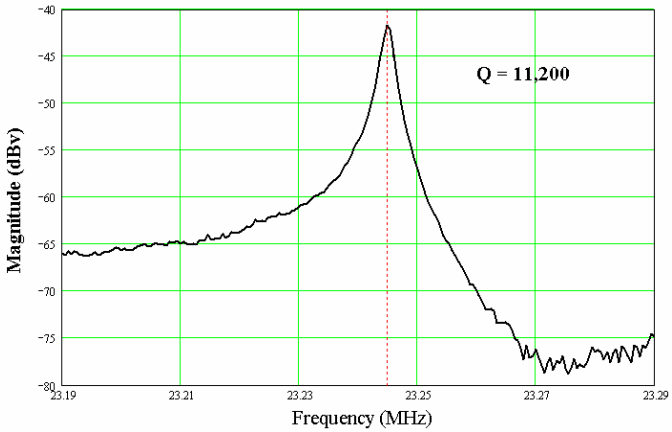

Figure 5.4: Frequency response of 100 μm disk resonator with 150 μm long quad-symmetric support beams

Table 5.4: Measured Q factors from the first batch prototypes

Resonator size W	100 μm			80 μm			60 μm
Beam length (b = 5 μm)	110 μm	130 μm	150 μm	50 μm	90 μm	130 μm	30 μm
Estimated Qs in air	7763	8662	10766	5364	6248	7010	6178
Measured Qs in air	**2000**	**4480**	**11200**	**3000**	**5700**	**6500**	**3490**

Table 5.5: Measured Q factors from the second batch prototypes

Resonator size W	80 μm		60 μm	40 μm	
Beam length (b = 2 μm)	48 μm	*5 μm*	41 μm	38 μm	*5 μm*
Estimated Qs in air	16636	*3824*	12789	19254	*4467*
Measured Qs in air	**7031**	***3114***	**6515**	**3300**	***2777***
Estimated Qs in vacuum	90600	*4712*	27800	55850	*5267*
Measured Qs in vacuum	**15248**	***3504***	**10061**	**9380**	***4218***

Over all from the above data, the analytical damping models presented in Chapter 4 yields larger Q factors than the measured ones. This implies that the analytical Q models underestimate the energy dissipations in the disk resonator system. This can be explained by the two assumptions made in the theoretical damping model: first, the disk is considered in pure shear stress state, so it suffers no thermal elastic damping; second, when resonating, the disk only has in plan movement, there is no out-plane movement and bending mode deformations. But in the real world, the conditions are not ideal and the above assumptions may not be hold. Thus, for a real device the thermal elastic and air damping can be more severe than that predicted by the ideal model. Plus, the theoretical modeling ignores other energy dissipation sources such as surface loss, end edge air damping, and defect loss.

Nevertheless, the measured quality factors followings the trend of the predicted Q factors very well. Specifically, when the support beams are short, the measured Qs are closely followed with the predicted values. Since, in this situation, the energy dissipation source in the disk resonator is dominated by the anchor loss of the support beams, and this loss mechanism is well described in the analytical model. Another situation is when the beam width is too wide, like in the prototype from first batch (b=5μm), the anchor loss from the support beams increases dramatically and becomes the dominant energy loss mechanism. From Table 5.2, one can see the strong influence of the anchor beams on the quality factors. These observations agree with the anchor loss model – equation (4.11), which shows that the energy transmitted through the anchor to the substrate is proportional to $(b/L)^3$.

The product of resonance and quality factor (f_rQ) is a good index to evaluate the performance of a resonator. Based on the measured data in Table 5.3, and 5.4, we obtained the average f_rQ products of the AlGaAs disk resonators:

at atmosphere $f_rQ = 2.11 \times 10^{11}$

in vacuum $f_rQ = 4.85 \times 10^{11}$

Comparing to the extensional AlGaAs bar resonator [17], the above f_rQ values are double of the correspondent f_rQs of bar type resonators when operating at fundamental mode.

From both the motional resistance measurements and the Q measurements, one can see the strong influence of the support beams, especially when the beam is very short or very wide. One interesting exercise can be conducted here: if only consider the anchor loss as the damping mechanism, what the optimal beam length should be? It is known that the electric resistance of the support beam is

$$R_p(L) = 2 \cdot \frac{\rho_e \cdot L}{b \cdot thic} \tag{5.2}$$

where: ρ_e is the resistivity of the $Al_{0.3}Ga_{0.7}As$:Si electrode layers;

thic is the thickness of the electrode layer.

Also the motional resistance can be calculated based on the Butterworth-Van Dyke equivalent circuit shown in Figure 2.10,

$$R_{anx}(L) = \frac{\omega_r \cdot M_e}{Q_{an}(L) \cdot \eta^2} \qquad (5.3)$$

where: $Q_{an}(L)$ is the quality factor due to the beam anchor loss and defined by equation (4.11).

The electric parasitic resistance R_p is proportional to the beam length L, while the motional resistance determined by anchor loss R_{anx} is proportional to $(1/L)^3$. The goal of optimization is to find the minimum value of (R_p+R_{anx}). Using the second batch 80μm disk resonator as the example, the (R_p+R_{anx}) vs. the support beam length L is obtained and shown in Figure 5.5. In this case, the optimal beam length is identified as: L= 9.7μm. In reality, however, increasing the support beam length not only yields lower anchor loss, but it also alters other energy losses and this effect is hardly determined analytically. Therefore, the eventual search for the optimal support beam length has to combine with experimental measurements.

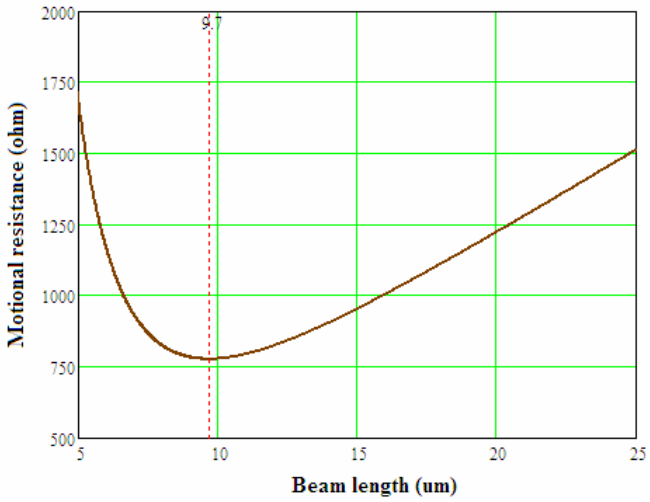

Figure 5.5: Beam length vs. the motional resistance due to anchor loss and support beam impedance

5.4 Temperature Stability

Temperature induced resonant frequency drift for the 80 μm and 100 μm resonators was measured from room temperature to 95 °C. The results are presented in Figure 5.6. It shows a good linear relation between the resonance and temperature, this will facilitate the temperature compensation in applications. The temperature coefficient of frequency (TCF) for the disk resonators should be independent of resonant frequency. As expected, the interpolated TCF is similar for the two resonators, with an average TCF of -46.0 ppm/°C. This value is comparable to other microfabricated resonators, although significantly larger than that of AT-cut quartz crystal resonators [49]. This thermal drift of resonance has been proved that is largely due to the temperature dependence of Young's modulus of thin film $Al_{0.3}Ga_{0.7}As$ [17]. Frequency stabilization and compensation schemes may ultimately be needed to minimize temperature-induced frequency drifts of the AlGaAs resonators.

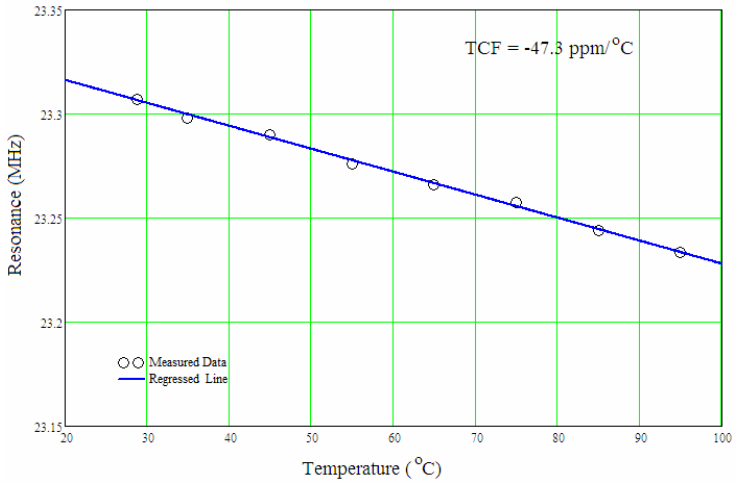

(a)

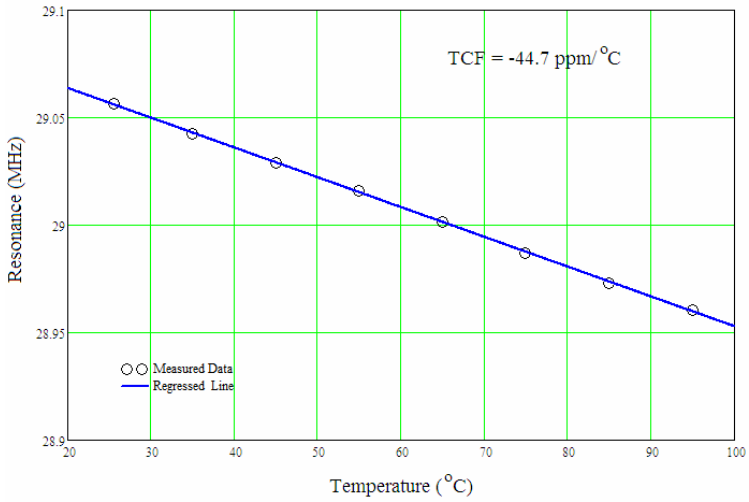

(b)

Figure 5.6: Measured temperature-induced frequency drift for (a) 100 μm and (b) 80 μm piezoelectric disk resonators

5.5 Power Handling Capability

The ability of a resonator to handle practical power levels is an important parameter in real-world application. To assess the power handling limits of the AlGaAs disk resonators, the devices were driven by the network analyzer with incremental power level increases. The frequency responses of the resonators were observed and the power limit is determined when the nonlinear behavior showed up. Figure 5.7 shows the measured response curves of an AlGaAs bar resonator at different power levels from previous work [17]. Apparently, when the input power is 10 dBm (actual power on the resonator is -6 dBm), the frequency response starts to exhibits nonlinear phenomenon.

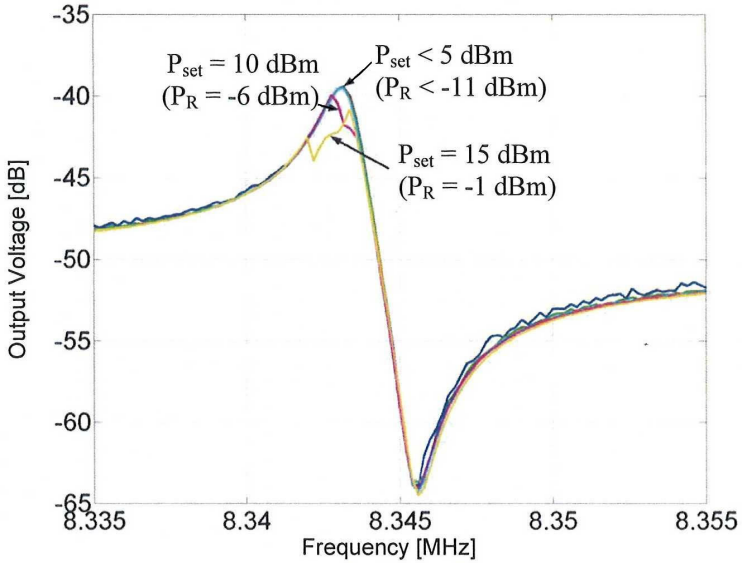

Figure 5.7: Transmission response of an AlGaAs bar resonator at various input power [17]

It has to point out that the power level set by the network analyzer is applied through a standard 50 Ω source resistance, and it generates an appropriate driving signal based on the assumption of a matched 50 Ω load resistance. But, in our cases, the impedance of the disk resonator is much larger than 50 Ω and it forms a voltage divider with the 50 Ω input resistance of the measurement instrumentation. Consequently, the actual power shared by the resonator is greatly reduced. The actual power P_R carried by the disk resonators can be calculated by,

$$P_R \approx 4P_{set}\frac{R_s}{R_x} \tag{5.4}$$

where: R_s is the source impedance of the instrument (R_s = 50 Ω);

R_x is the motional resistance of the microresonator ($R_x >> R_s$);

P_{set} is the instrument set-up power.

Figure 5.8, 5.9, and 5.10 shows the measured frequency responses at different power levels of the 80 μm, 60 μm, 40 μm AlGaAs disk resonators, respectively. It is observed that up to the maximum power level -- 15 dBm of the network analyzer, there are no prominent nonlinear behaviors occurring in these microresonators. Assuming 15 dBm is the maximum input power in the microresonator test set-up, according to equation (5.4), the actual power levels dissipated on the microresonators are calculated as:

for 80 μm resonator, P_R = 1.9 dBm

for 60 μm resonator, P_R = 2.5 dBm

for 40 μm resonator, P_R = 2.1 dBm

These power handling values correspond to the absolute power level about 1.6 mW. To our knowledge, this is the highest power handling capability in the published microresonators. Compared to the AlGaAs bar resonator developed in previous work [17], the power handling level is improved by an order of magnitude. In fact, these power handling levels are very close to the GSM communication requirements. Further improvements in power handling can be realized by increasing AlGaAs plate thickness or utilizing multiple resonators connected in parallel, although the trade-offs of these measures are that the motional resistance increase or the complexity of fabrication.

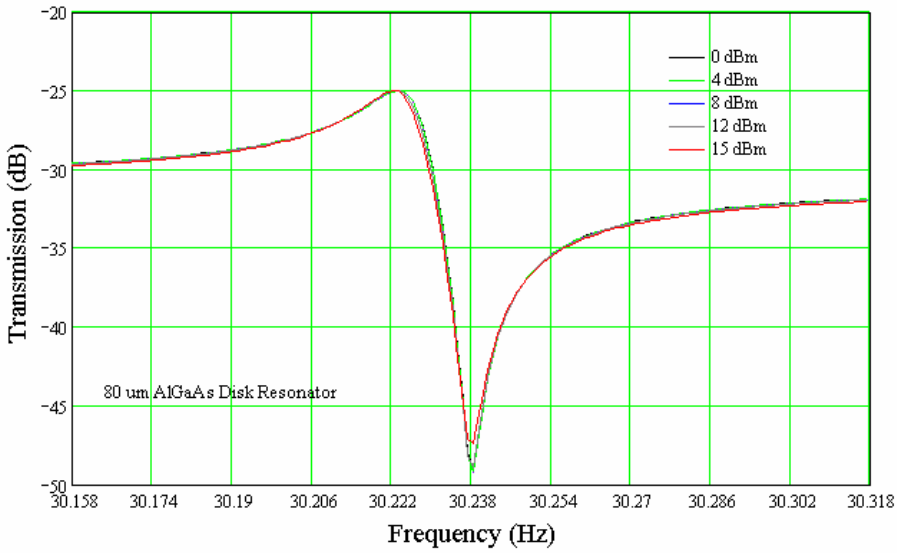

Figure 5.8: Transmission response of 80 μm disk resonator at various input power level

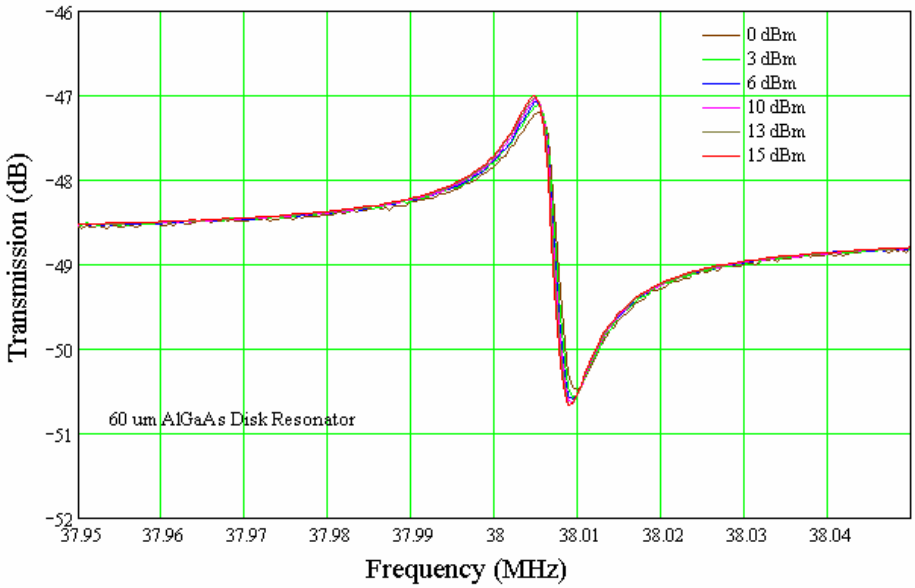

Figure 5.9: Transmission response of 60 μm disk resonator at various input power level

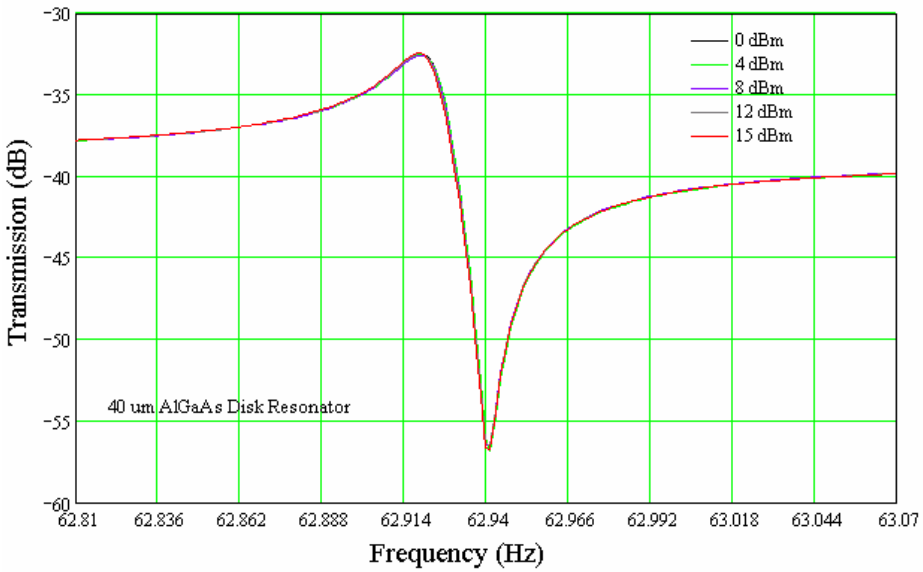

Figure 5.10: Transmission response of 40 μm disk resonator at various input power level

Chapter 6 : Two-port Filters Based on AlGaAs Disk Resonator

6.1 Introduction

Filters are crucial components in RF and microwave circuits, which can select the signal from all the additional signals before it is processed. A filter can be formed by multiple single-port resonators which act as simple impedance elements, such as the ladder type band-pass filter [50]. A more direct approach to realizing RF filters based on MEMS resonators is through the use of two-port resonator elements. Two-port resonators are attracting significant attention for development high performance MEMS filters [1, 3, 4, 7, 12, 13, 51, 52]. Figure 6.1 and 6.2 illustrate a two-port piezoelectric beam resonator design by Piekarski et al. [52] and a capacitive disk filter design by Pourkamali et al. [1], respectively. In application, the RF electric signal is applied to the input port of the filter, which excites the mechanical resonator structure, subsequently the electric signal is transformed into the mechanical energy. On the output port of the filter, the electrode through electromechanical transduction senses the resonating mechanical energy and converts it back into electric energy. By the means of the high Q factor of a mechanical resonator, the electric signal is selectively passed through this two-port device.

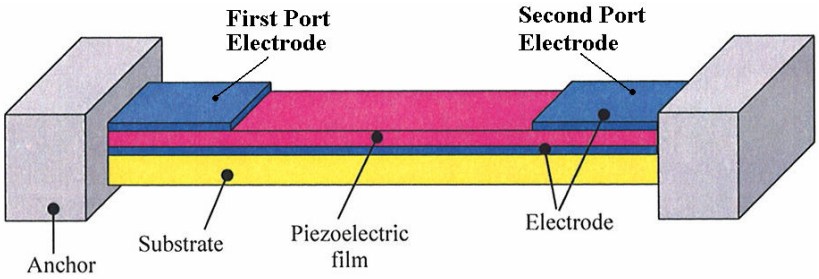

Figure 6.1: Schematic of two-port piezoelectric beading mode resonator [52]

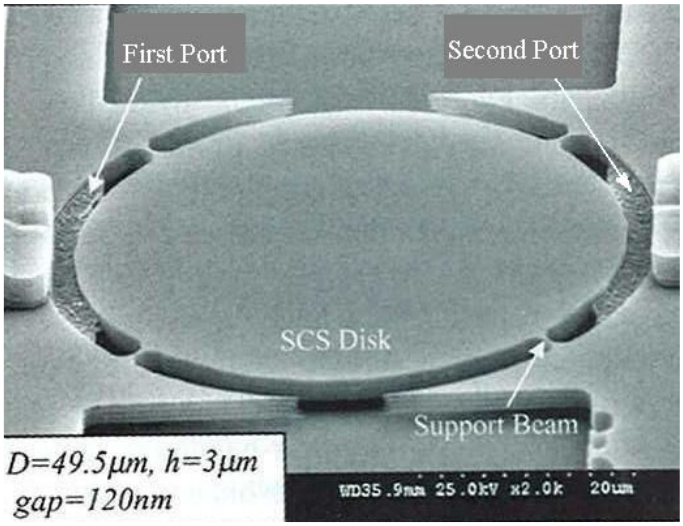

Figure 6.2: SEM picture of a reported two-port silicon disk resonator [1]

However, no two-port resonator designs based on a piezoelectric, 2-D, contour-mode resonator have been reported in the literatures. In this chapter, the design and fabrication of two-port AlGaAs disk resonators is described. Two different electrode configurations are considered. The working principles of both designs are verified by the FEA models in ANSYS 8.0. An equivalent circuit model for the two-port resonators is also developed, and the analytical transfer function is derived with the aid of electric net-work theory. Experimental results of fabricated 2-port resonator prototypes are presented. The theoretical model is verified by these test results. Furthermore, the optimal electrode design of the two-port resonator is determined.

6.2 *Filter Design Based on AlGaAs Disk Resonator*

To make a filter out of the disk resonator, two electrically separated electrodes have to be placed on the top surface of the AlGaAs disk. One electrode is served as the input port, the other as the output port. Meanwhile, the bottom electrode layer is remained solid and connected to the ground of the circuit. To minimize the impact of the electrode pattern to the resonant mode shape, the layout of the top electrode should be kept in good symmetry. Two different electrode patterns for the two-port filter have been designed, and they are illustrated in Figure 6.3.

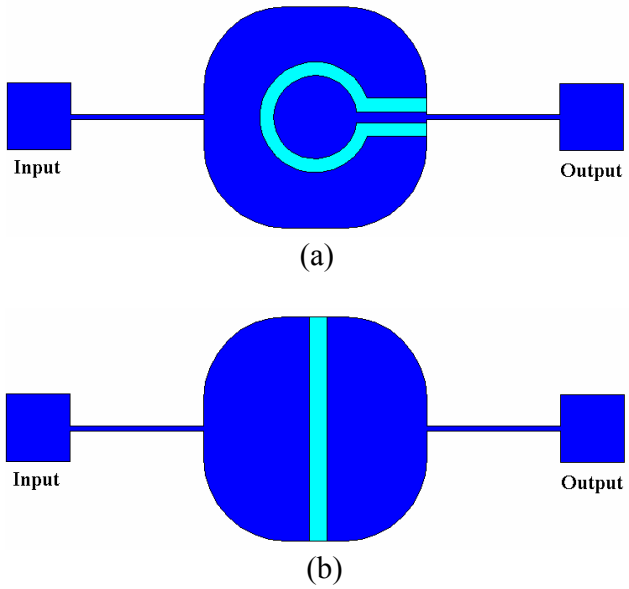

Figure 6.3: Two filter designs based on the disk resonator: (a) circular electrode pattern, (b) half plane electrode pattern

To verify these two electrode patterns, FEA simulations on the frequency responses between the input electrodes and the output electrodes are conducted in Ansys 8.0. Basically, a unit electric potential is applied to the input electrode, at different frequency the responding potential of the output electrode is obtained through the

FEA numerical simulations. Figure 6.4 presents the results from this FEA modeling. These frequency responsive curves are different from the one of a single-port resonator, which possesses a resonator peak and an anti-resonant peak. Only one prominent peak (correspondent to the resonance of the plate) shows in these frequency response curves, and it demonstrates a typical behavior of a filter.

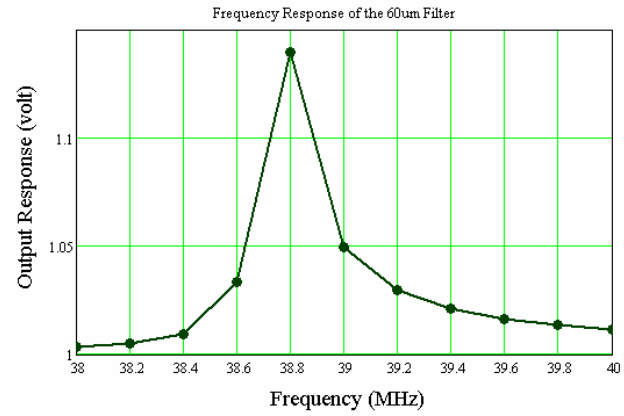

(a)

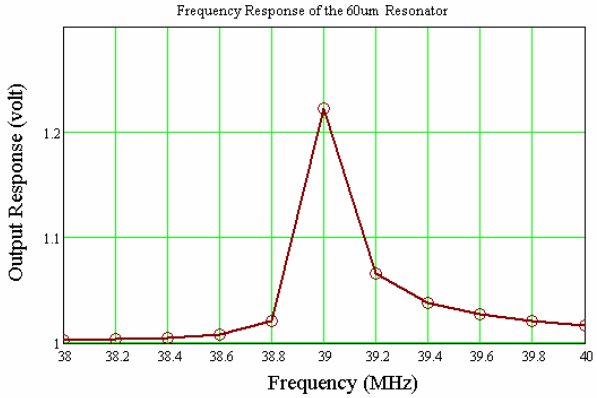

(b)

Figure 6.4: The FEA simulated frequency responses of the two proposed filter designs (a) circular pattern electrode (b) half plane pattern electrode

6.3 Equivalent Circuit of the Two-port Resonator

A piezoelectric device can be represented by an electric circuit with lumped, discrete L, R, C components. Doing so will help one to understand the device and bring insight to its working mechanism. Moreover, by means of the equivalent circuit, the

transfer function of the device can be easily derived with the aid of the electric network theory. The analytical formula of the transfer function will be a powerful tool for designers to optimize the performance and mathematically predict the behavior of the device. To this end, the equivalent circuit for the two-port filter has been developed and it is shown in Figure 6.5. From this circuit, it is vividly shown the input port (R_1, C_1) in coupled to the output port (R_2, C_2) through the mechanical resonator (L_m, R_m, C_m), and the transformers with ratio η_1, η_2 connect the mechanical domain to the electric domain.

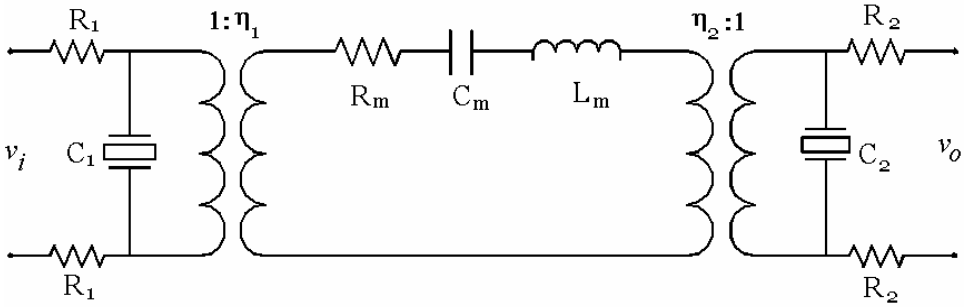

Figure 6.5: Equivalent circuit of the two-port AlGaAs 2D resonator

where: R_1, R_2 are parasitic resistance (mainly from the support beams);

C_1, C_2 are input, output port electric capacitance;

L_m, R_m, C_m are modal mass, damping coefficient, compliance, respectively;

η_1, η_2 are piezoelectric transduction coefficients of input and output port.

By applying the circuit network theory, the transadmittance $Y(\omega)$ between the input port and the output port of the filter is derived,

$$Y(\omega)=\frac{i_o}{v_i}=\frac{\eta_1\cdot\eta_2}{R_1\cdot\left[\eta_1^2+j\omega C_1(Z_m(\omega)+\eta_2^2 Z_2(\omega))\right]+(Z_m(\omega)+\eta_2^2 Z_2(\omega))}\cdot\frac{1}{(1+j\omega R_2 C_2)} \tag{6.1}$$

where: mechanical branch impedance $Z_m(\omega)=\frac{1}{j\omega C_m}\cdot\left[1-\left(\frac{\omega}{\omega_0}\right)^2+j\cdot\frac{1}{Q}\left(\frac{\omega}{\omega_0}\right)\right]$

output port impedance $Z_2(\omega)=\frac{R_2}{1+j\omega R_2 C_2}$

Plug the typical values from the 60μm two-port resonator into the equation (6.1), the transadmittance response curve can be plotted in the frequency domain and it is given in Figure 6.6. The sharp peat at the filter resonance indicates that this new filter design offers very good frequency selectivity.

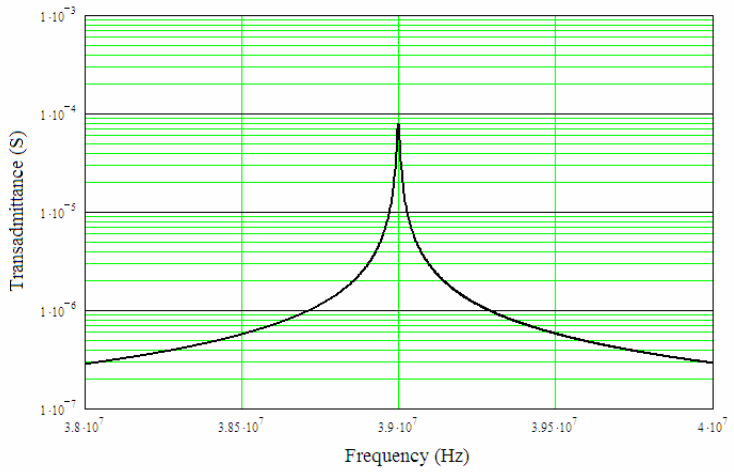

Figure 6.6: Transadmittance response in vicinity of resonance

When C_1 and C_2 are small (in our devices C_1 & C_2 << 1pF), $j\omega R_1C_1 \approx 0$, $j\omega R_2C_2 \approx 0$, and $Z_2(\omega) \approx R_2$, the transadmittance expression (6.1) can be greatly simplified,

$$Y(\omega)=\frac{\eta_1\cdot\eta_2}{Z_m(\omega)+\eta_1^2\cdot R_1+\eta_2^2\cdot R_2} \tag{6.2}$$

And at resonance,

$$Y(\omega_0) = \frac{\eta_1 \cdot \eta_2}{R_m + \eta_1^2 \cdot R_1 + \eta_2^2 \cdot R_2} \qquad (6.3)$$

Clearly, the parasitic resistance R_1 and R_2 contribute to the final resonance impedance (motional resistance R_x), and lower the resonator Q factor.

6.4 Electrode Optimization

Transduction coefficient η_1, η_2 that are associated to the first electrode port and the second electrode port are the measure that how well the mechanical resonator can convert its mechanical energy into electric energy and vice versa. According to the definition of piezoelectric transduction coefficient,

$$\eta = \frac{I(j\omega)}{V(j\omega)} = \frac{\int_A d_{ikl} T_{kl} \cdot j\omega \cdot dA}{d_{\max} \cdot j\omega} \qquad (6.4)$$

For a normalized resonance mode, η_1, η_2 can be calculated as,

$$\eta_1 = \int_{A1} \tau_{xy}(x,y) \cdot d_{36} \cdot dA$$

$$\eta_2 = \int_{A2} \tau_{xy}(x,y) \cdot d_{36} \cdot dA \qquad (6.5)$$

where: *A1, A2* are the areas of input port and output port respectively;

$\tau_{xy}(x,y)$ the shear stress field of the resonant mode;

d_{36} the piezoelectric coefficient of AlGaAs.

If there is no gap between input electrode and output electrode, then the 2-D plate area $A = A1+A2$, which leads to:

$$\eta_T = \int_A \tau_{xy}(x,y) \cdot d_{36} \cdot dA = \eta_1 + \eta_2 \qquad (6.6)$$

where: η_T is the total transduction coefficient of the resonator plate.

Substitute equation (6.5) into equation (6.3) and replace η_2, the transadmittance at resonance becomes,

$$Y(\eta_1) = \frac{\eta_1 \cdot (\eta_T - \eta_1)}{R_m + \eta_1^2 \cdot R_1 + (\eta_T - \eta_1)^2 \cdot R_2} \tag{6.7}$$

To find the maximum of $Y(\eta_1)$, one can set the first order derivative of $Y(\eta_1)$ to equal zero, and obtains: $\eta_1 = \frac{1}{2}\eta_T$ (6.8)

This implies that when the transduction coefficient of input electrode equals to that of the output electrode (i.e. $\boldsymbol{\eta_1 = \eta_2}$), the transadmittance of the filter reaches the maximum value. In other word, the insertion loss of the two-port filter achieves its minimum value at this condition. This important conclusion is further validated by the measurement results.

6.5 Prototyping and Verification

The prototypes of the two-port resonator using both the electrode designs are fabricated based on the 60μm single port AlGaAs resonator. The fabrication process is exactly same as the one for the single port AlGaAs resonator described in Chapter 3, with the only difference in the pattern of the top electrode mask. Three different geometries of the circular two-port electrode design are employed in attempt to observe the trend of the electrode area on the performance of the filters. The details of the circular electrode designs are illustrated in Figure 6.7. The prototype of the half plane electrode design is also show in Figure 6.8.

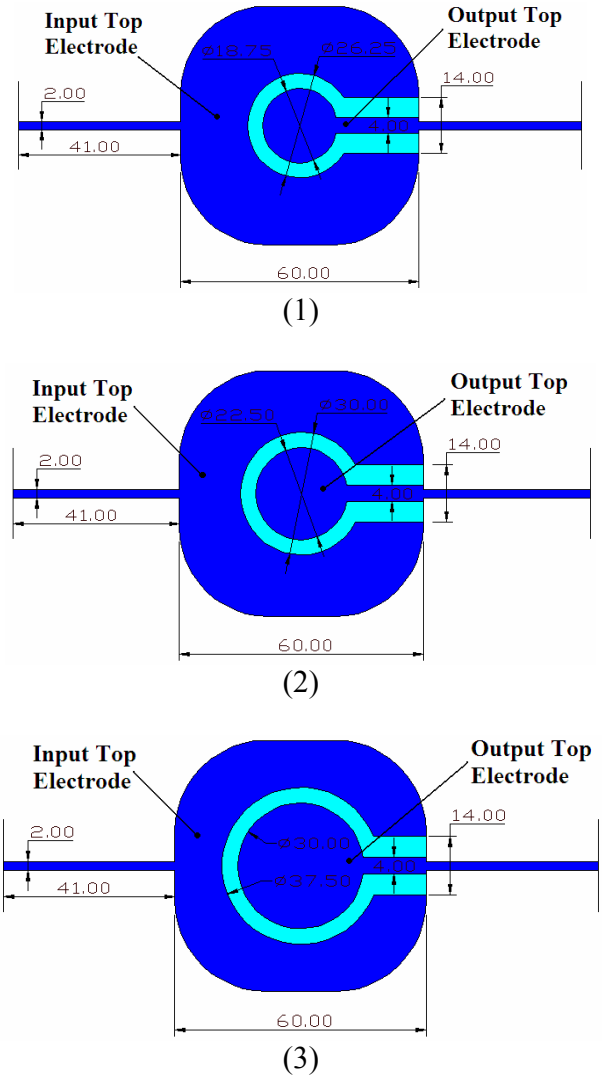

Figure 6.7: Three different prototypes of circular electrode pattern based on 60µm $Al_{0.3}Ga_{0.7}As$ plate

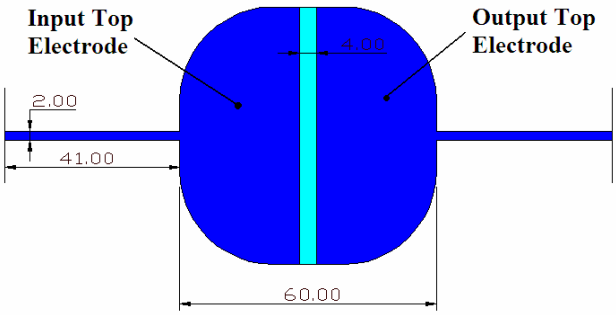

Figure 6.8: Prototype dimensions of the half plane electrode design

Two perspective views of the finished filter prototypes are presented in Figure 6.9.

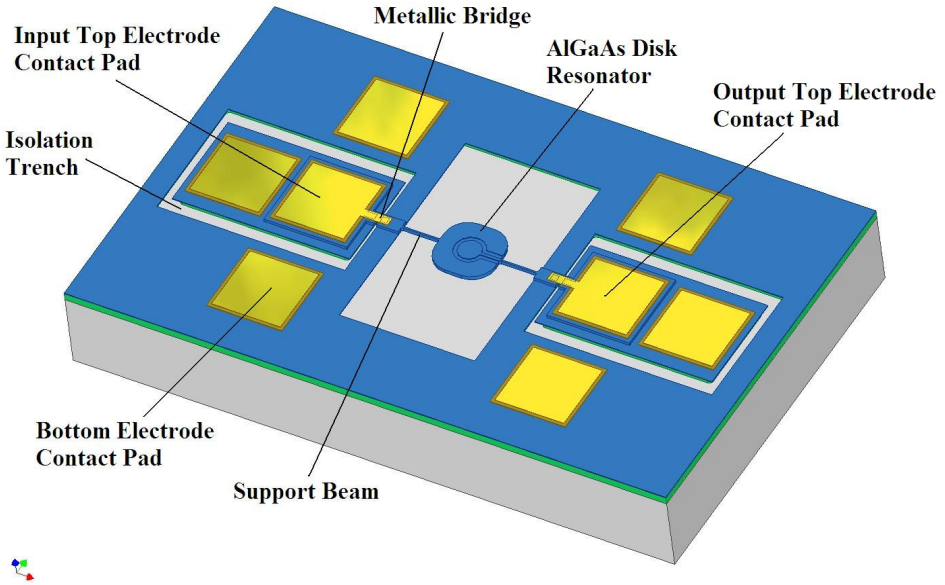

(a)

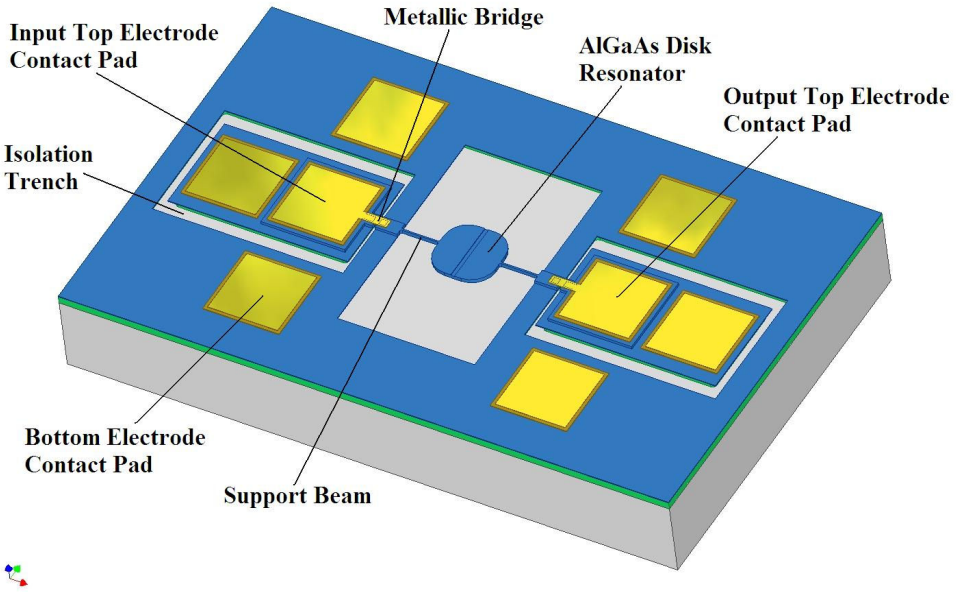

(b)

Figure 6.9: Persepective views of the fabricated two-port resonators (a) circular electrode design (b) half plane electrode design

The transmission frequency responses of the prototype filters are directly measure by a network analyzer (HP 4395A). The input port of the filter under test is connected with the source output of the network analyzer which generates sinusoidal RF signal; the output port of the filter is directly connected to the 50Ω input port of the network analyzer. The transfer function of the device is obtained through the scanning the input RF signals in the interested frequency range. Three major parameters of the filter can be derived from this measurement, i.e. resonance frequency, motional resistance, and quality factor Q. The measurements are conducted both in atmosphere pressure and in vacuum condition (pressure 60μTorr).

Figure 6.10 and 6.11 shows the measured transmission curves in vacuum of the filters with the circular electrode pattern and half plane electrode pattern respectively. Table 6.1 summarizes the results of all the prototypes from the transmission tests. It is seen that the filters with the half plane electrode design have lowest insertion loss (motional resistance) among all the prototypes we build. Regarding the filters of circular electrode pattern, the layout (2) in Figure 6.7 yields the smallest insertion loss. In general, for all the prototypes the insertion losses measured in vacuum condition are lower than that measured in atmosphere.

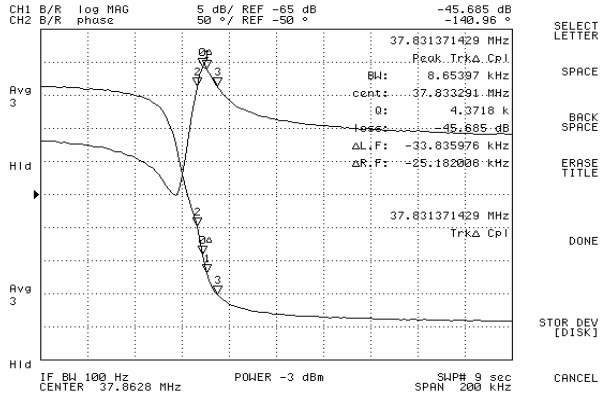

Figure 6.10: Transmission response of the 60μm filter with circular electrode layout (2) in vacuum (resonance @ 37.83 MHz)

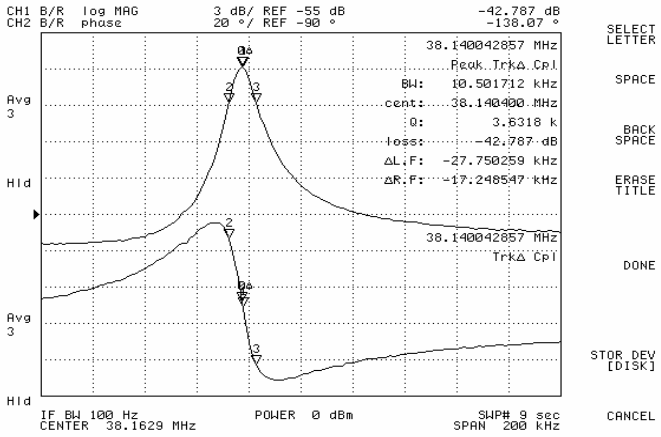

Figure 6.11: Transmission response of the 60μm filter with half plane electrode layout (resonance @ 38.14 MHz)

Table 6.1: Measured insertion loss (IL) and Q factors of the prototype filters

	Circular Pattern				Half Plane Pattern	
	Layout(1) IL	Layout(2) IL	Layout(3) IL	Q factor	Layout(1) IL	Q factor
in atmosphere	-48.5 dB (13.3 kΩ)	-47.5 dB (11.8 kΩ)	-50.3 dB (16.3 kΩ)	2700	-43.9 dB (7.8 kΩ)	2390
In vacuum	-47.0 dB (11.1 kΩ)	-45.7 dB (9.6 kΩ)	-48.2 dB (12.8 kΩ)	4372	-42.8 dB (6.9 kΩ)	3632

The lower insertion loss associated with the half plane design can be explained as that: first, the half-plane electrode configuration automatically satisfies the optimal electrode condition $\eta_1 = \eta_2$; second, the gap between the input and output electrode takes less area than the circular electrode configuration does, thus, the half-plane design more efficiently uses the area of the 2-D resonaotr, resulting in the higher piezoelectric transduction coefficients. In fact, the FEA simulation shows that

$$for\ half-plane\ pattern: \quad \eta_T = \eta_1 + \eta_2 = 1.75 \times 10^{-5}\ (N/V)$$

$$for\ circular\ pattern: \quad \eta_T = \eta_1 + \eta_2 = 1.50 \times 10^{-5}\ (N/V)$$

Therefore, according to the transadmittance equation (6-7), the prototype with the half-plane electrode design will have the lowest insertion loss among any of the three prototypes with circular electrode configurations. In general, one can draw the conclusion that the halp-plane electrode design is more efficient than the circular electrode design.

Among the circular electrode prototypes, the layout (2) is more close to the optimal electrode condition -- $\eta_1 = \eta_2$, according to equation (6.3), it should give higher transadmittance. To further verify the theoretical model, we plug the calculated as well as the FEA determined η_T in the equation (6.3), and plot the curve of insertion loss vs. transduction coefficient η_2 against the measured results from the prototypes of the three circular electrode layouts in Figure 6.12. Fairly good agreement between the theoretical curve and the measured results is demonstrated. Clearly, the layout (2) is more close to the optimal condition.

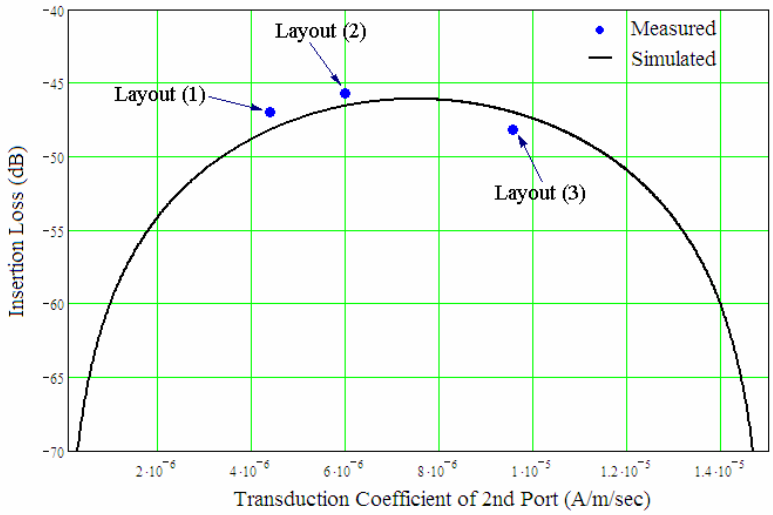

Figure 6.12: Transduction coefficient η_2 vs. insertion loss

Comparing to the single port resonator, the insertion losses of the 2-port filter are larger. This phenomenon can also be explained from the admittance formula (6.3). The additional resistance R_1 and R_2 from the support beams contribute to the final impedance of the filter and they are doubled the value of the parasitic impedance of a single port resonator if same support beam length is used. R_1 and R_2 as the electric loss element can also lower the measured Q values. By choosing an optimal support beam length, one can dramatically improve the insertion loss of this filter and increase the Q factors as well.

Chapter 7 : Conclusions and Future Work

7.1 *Single Port 2-D AlGaAs Resonator*

A new design for anisotropic piezoelectric disk resonators has been developed. The shape of the disk resonator is based on the velocity propagation profile of the elastic wave in the plane of the piezoelectric film, with lateral dimension scaled to the half wave length of the desired resonance frequency. FEA model for this new design is created in Ansys 8.0 software. The simulated frequency responses validate the design concept of the 2-D resonator. Moreover, the parameters extracted from the FEA model show that this new 2-D resonator has better performance than the beam type counterparts. The prototypes of the new resonator are realized based on single-crystal $Al_{0.3}Ga_{0.7}As$ films. The well characterized epitaxial $Al_xGa_{1-x}As$ films possess moderate piezoelectric coupling coefficients. Moreover, to take the advantage of the low loss single crystal $Al_{0.3}Ga_{0.7}As$ film, the heterostructure of the Si doped $Al_{0.3}Ga_{0.7}As$ films on top and bottom of an undoped $Al_{0.3}Ga_{0.7}As$ piezoelectric layer is employed. A unique 7-mask MEMS fabrication process has been developed and successfully implemented to make the prototypes of the new disk resonators. One salient feature in this process is the insolated contact pads and a metal bridge jump over the top electrode of the disk to the top contact pad. This feature greatly reduces the parasitic capacitance between the top and bottom contact pads and provides higher single-to-noise ratio in the measurements.

The prototypes of the disk resonators are made with the resonance frequencies varying from 24 MHz to 62 MHz. Different support beam lengths are also tried in order to assess their effect on the Q factors. Three major energy dissipation sources in this disk resonator system, namely anchor loss, thermal elastic loss, and air damping, are well described and modeled. Comparing to the measured Q factors with the estimated Q factors from the energy dissipation models, it is found that the Qs from the resonators with short support beams (5μm) are reasonably close to the analytical predictions, but, the Qs from the ones with longer support beams are much less than the analytical predictions. In the case of short support beam, the anchor loss through the support structure is the dominant energy dissipation source and this damping mechanism is well modeled in the analytical solution. Whereas, in the cases of slender long support beams, the out of plane movement and bending vibration modes are inevitably introduced, thus the assumption of pure in-plane shear resonating mode in the disk resonator is not held any more, consequently the thermal elastic damping and air damping are significantly increased, making the estimated Qs based on the ideal conditions too optimistic. These rocking and bending movements, however, are difficult to be modeled analytically. In terms of achieving higher Q factors, the optimal beam length seems between the 5μm and 40μm (Refer to Table 5.3). In short, the Q calculation models presented in this work captures the essence of the damping phenomena in the disk resonator system, and they provide good design guidance and foundation for further optimization of the support structure.

The measured results from the prototypes of the disk resonator are very encouraging. In specific, the best performances obtained in atmosphere from the prototypes are: a Q factor of 7031 at 30.2 MHz with 1.11 kΩ intrinsic motional resistance, a Q factor of 6515 at 40.8 MHz with 1.26 kΩ intrinsic motional resistance, and a Q factor of 3300 at 62.3 MHz with 2.43 kΩ intrinsic motional resistance. The measured power handling level is about 1.6 mW. Regarding all the above performance aspects, the disk resonator outperforms the extensional mode bar resonator. The measured temperature stability of the $Al_{0.3}Ga_{0.7}As$ disk resonator is about -47 ppm/^{o}C, which is equivalent to that of the beam type counterpart and is comparable to that of the Si capacitive resonators. The high Q and low motional resistance R_x demonstrated by this disk resonator indicate that this disk resonator possesses a dominant resonating mode and this mode traps more energy than the beam type counterparts.

7.2 Two-port 2-D AlGaAs Resonator

To take the advantage of the high quality disk resonator, two-port piezoelectric resonators, i.e. filters, are developed based on the $Al_{0.3}Ga_{0.7}As$ disk resonator. Two unique electrode patterns are designed on the top electrode surface of the disk resonator. FEA simulations reveal that both designs have a typical filter response -- a single resonant peak in frequency domain. Theoretical equivalent circuit model for these filters is created with the parameters derived from the FEA results. From the transadmittance function of the equivalent circuit, the conclusion on the optimal input and output electrode design is obtained, that is to arrange the two electrodes so that the piezoelectric transduction coefficients of the input and output electrodes are equal.

Obviously, the symmetric half plane electrode pattern automatically satisfies this condition. Regard the circular electrode design, careful arrangement of the electrode geometries have to be conducted in order to meet this optimal condition. Prototype filters with three different circular electrode layouts and one half plane electrode pattern are fabricated using the same process developed for the $Al_{0.3}Ga_{0.7}As$ disk resonator in this work. Very good performances are demonstrated by these prototypes, that are summarized here: for the circular patter design, the best insertion loss reaches -45.7 dB correspondent to gross motional impedance 9.7 kΩ at 37.8 MHz with quality factor 4372; for the half plane electrode design, the best insertion loss reaches -42.8 dB correspondent to gross motional impedance 6.9 kΩ at 38.1 MHz with quality factor 3632. The measured insertion losses from the three different circular layouts reasonably agree with the analytical predictions based on the equivalent circuit, which validates the optimal electrode condition retrieved from the analytical equation (6.6). The fact that the fundamental resonant mode of the 2-D $Al_{0.3}Ga_{0.7}As$ disk is easily excited by either input electrode designs indicates that the 2-D plate with the propagation velocity profile of acoustic wave possesses a strong and dominant resonant mode and the electric signal can be efficiently transferred from the input electrode to output electrode through this resonant mode.

7.3 Future Work

While the $Al_{0.3}Ga_{0.7}As$ disk resonators developed in this work outperform their beam type counterparts, there remain substantial areas for improvement. For instance, as it is shown in the prototype measurements, when the support beams are very short (as in

the cases of 5μm long support beams), the resonator suffer greatly from the anchor loss and this loss mechanism dominates all the other energy dissipation sources, resulting in the low quality factor of the 2-D resonator system. On the other hand, if we increase the length of the support beams, according to the theoretical model (equation 4.11) the anchor loss will reduce rapidly. However, if the beam length is too long, the series electric resistance from the electrode layers of the support beams becomes a major energy loss source and this parasitic impedance is eventually reflected on the final motional resistance of the resonator. In addition, very long support beams can induce out-of-plane movement and bending deformation in the 2D plate which will dramatically increase the TE damping and air damping. These adverse effects will override the benefit of the reduction of anchor loss and end up with the quality factor much lower than what one expected. Therefore, there must be a beam length in between the short and long beams used in the prototypes, which will produce minimum energy dissipation and have tolerable parasitic impedance. If only the anchor loss and the parasitic electric resistance of the support beams are considered as the design factors, the optimal beam length can be easily found by the anchor loss formulae (4.11) combined with the equation of the electric impedance of the support beam, which is discussed in Chapter 5. But, in reality other loss sources will be introduced by the long support beam and this part of loss mechanism is difficult to be modeled analytically. Thus, experimental tests have to be conducted in the search of the optimal support beam length. Naturally, determining the optimal support beam length at a specific resonance frequency is one important topic for future work.

The motional resistance of the $Al_{0.3}Ga_{0.7}As$ disk resonator is several folds lower than that of a beam type counterpart, but it is still much higher (in kΩ range) than the standard impedance – 50 Ω impedance of current RF devices. This impedance mismatch presents a hurdle to integrate these MEMS resonators and filters with the current standard RF systems. However, it has been demonstrated that a mechanically-coupled and electrically connected in parallel resonator array can substantially reduce the motional resistance and also improve the power handling capability [53, 54]. Figure 7.1 and 7.2 shows the successful attempts in this approach which combine multiple high-impedance capacitive resonators to form a resonator array and much lower motional impedances are achieved. In [53, 54], it has shown that the impedance reduction is approximately equal to the reciprocal of the number of resonator used. This approach should be also applicable to the piezoelectric MEMS resonators. The challenge to implement this solution on the $Al_{0.3}Ga_{0.7}As$ disk resonators is how to mechanically couple the 2-D resonators so that only one strong vibration mode ends up in this array, making it function as a single resonator. The mechanical coupler and location for the coupler in the 2-D resonator plate have to be carefully designed and selected. If this is achieved, then the road for the disk resonators and filters to be integrated with the current standard RF systems is paved. This will likely be an important topic for the future research.

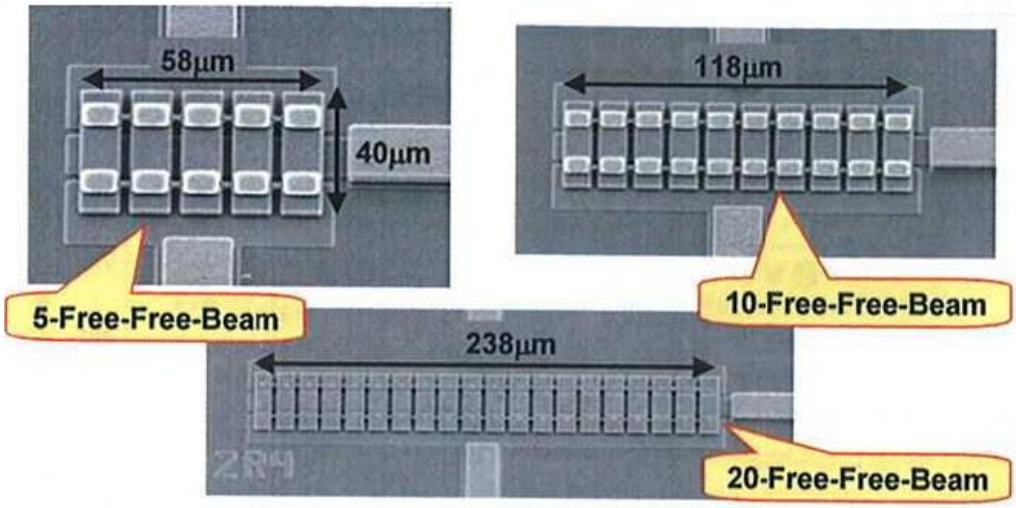

Figure 7.1: Mechanically coupled Si beam resonator array [53]

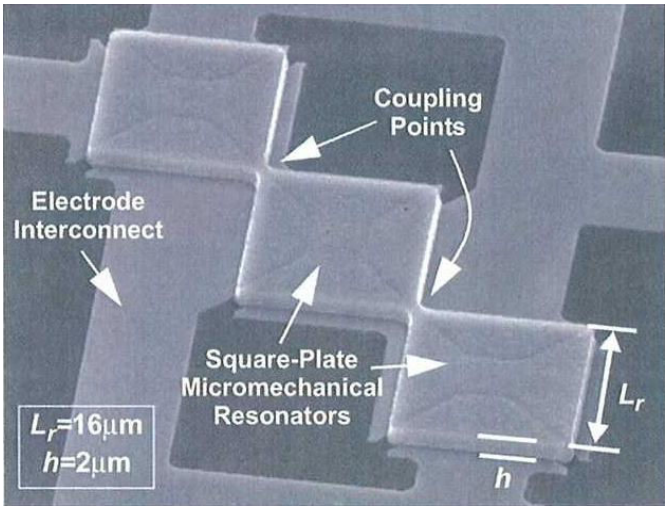

Figure 7.2: Mechanically-coupled Si plate resonator array [54]

Appendix A

Matlab program for elastic wave velocity calculation of AlGaAs crystal

```
clear all; close all;
% Calculate Christoffel tensor and its eigenvalues
% To obtain the phase velocity profile in (100) plane of AlGaAs crystal
% Ken Deng
% Last modification: June 15, 2004
% Email: kenkdeng@yahoo.com

% Program layout:
% 1) Assign stiffness matrix(6x6) and convert to tensor
% 2) Assign piezoelectric matrix(3x6) and convert to tensor
% 3) Assign dielectric matrix (3x3)
% 4) Define the direction vector (1x3) in X-Y plane
% 5) Calculate the Christoffel tensor (3x3) ---- Main Task
% 6) Calculate the eigenvalues of the Christoffel tensor
% 7) Save the three phase velocities (sqr'eigenvalue/rho') in a data file
% 8) Increase the direction angle and go back 4)

% 1) Define standard stiffness matrix
C=zeros(6,6);
c11=118.8+1.4*0.3;   % AlGaAs stiffness variables
c12=53.88+3.2*0.3;   % unit: GPa
c44=59.4-0.5*0.3;      % cubic crystal system
C(1,1)=c11;
C(2,2)=c11;
C(3,3)=c11;
C(4,4)=c44;
C(5,5)=c44;
C(6,6)=c44;
C(1,2)=c12;
C(1,3)=c12;
C(2,3)=c12;
C(2,1)=c12;
C(3,1)=c12;
C(3,2)=c12;
C=C.*10^9,    % display the standard stiffness matrix (unit: Pa)

Cten=zeros(3,3,3,3);    % Convert to stiffness tensor
for i=1:3
   for j=1:3
```

```
      for m=1:3
         for n=1:3
            u=ten_mat(i,j);
            v=ten_mat(m,n);
            Cten(i,j,m,n)=C(u,v);
         end
      end
   end
end

% 2) Assign piezoelectric matrix(3x6) and convert to tensor
D=zeros(3,6);
d14=2.69+1.13*0.3;   % AlGaAs piezoelectric coefficient (pC/N)
D(1,4)=-d14*10^-12;  % unit C/N
D(2,5)=-d14*10^-12;
D(3,6)=-d14*10^-12;
D,           % display the piezoelectric matrix
E=D*C,       % calculate the piezoelectric strain coefficient


Eten=zeros(3,3,3);    % Convert to piezoelectric tensor
for i=1:3
   for m=1:3
      for n=1:3
         v=ten_mat(m,n);
         Eten(i,m,n)=E(i,v);
      end
   end
end

% 3) Assign dielectric coefficient matrix(3x3)
Eps=zeros(3,3);
kappa=10.89-2.73*0.3;   % AlGaAs relative dielectric constant
eps0=8.85*10^-12;       % Absolute dielectric constant (F/m)
Eps(1,1)=kappa*eps0;
Eps(2,2)=kappa*eps0;
Eps(3,3)=kappa*eps0;
Eps,                % display the dielectric matrix

rho=5360-1600*0.3;      % density of AlxGa(1-x)As (unit: kg/m^3)

% 4) Define propagation direction vector
bdir=zeros(3,1);
theta=0;    iang=1;
darc=pi*5/180;          % 5degree increment
theta=(iang-1)*darc;
```

```
bdir(1)=cos(theta);     % (001)GaAs wafer
bdir(2)=sin(theta);
bdir,                   % display the direction vector

% open a file to save the eigenvalues(speed)
fdata=fopen('C:\KEN\Piezo_MEMS_Resonator\velocity_XY.txt','a+');
% File for reading, writing, and appending (a+)

% 4) Define propagation direction vector
theta=0;
darc=pi*5/180;          % 5degree increment
for iang=1:73
 bdir=zeros(3,1);
 theta=(iang-1)*darc;
 bdir(1)=cos(theta);     % (001)GaAs wafer
 bdir(2)=sin(theta);
 bdir,                   % display the direction vector

% 5) Calculate the Christoffel tensor Gamma(3x3)----Major Task
Ede=0;
for s=1:3
  for t=1:3
     Ede=Eps(s,t)*bdir(s)*bdir(t)+Ede;
  end
end

Gamma=zeros(3,3);

for j=1:3
   for k=1:3
      Gamma(j,k)=0;

      for i=1:3
       for l=1:3
        Eno=0;

          for m=1:3
           for n=1:3
              Eno = Eten(m,i,j)*Eten(n,k,l)*bdir(m)*bdir(n) + Eno;
           end
          end

        Gamma(j,k)=( Cten(i,j,k,l) + Eno/Ede )*bdir(i)*bdir(l) + Gamma(j,k);
       end
      end
```

```
   end
end

% 6) Calculate the eigenvalues of the Christoffel tensor
comm1='The Christoffel tensor is:',
Gamma,
comm2='The eigenvalues are:',
Ceig=eig(Gamma),

% 7) Save the three phase velocities(sqr'eigenvalue/rho') in a data file
v1=sqrt(abs(Ceig(1))/rho),
v2=sqrt(abs(Ceig(2))/rho),
v3=sqrt(abs(Ceig(3))/rho),
fprintf(fdata,'%7.3f,3%8.2f,\n',theta,v1,v2,v3);

end
fclose(fdata);
```

Bibliography

[1] S. Pourkamali, H. Zhili, and F. Ayazi, "VHF single crystal silicon capacitive elliptic bulk-mode disk resonators-part II: implementation and characterization," *Journal of Microelectromechanical Systems*, vol. 13, pp. 1054-1062, 2004.

[2] K. Wang, A. C. Wong, and C. T. C. Nguyen, "VHF free-free beam high-Q micromechanical resonators," *Journal of Microelectromechanical Systems*, vol. 9, pp. 347-360, 2000.

[3] V. Kaajakari, T. Mattila, A. Oja, J. Kiihamaki, and H. Seppa, "Square-extensional mode single-crystal silicon micromechanical resonator for low-phase-noise oscillator applications," *Electron Device Letters, IEEE*, vol. 25, pp. 173-175, 2004.

[4] F. D. Bannon, J. R. Clark, and C. T. C. Nguyen, "High-Q HF microelectromechanical filters," *Solid-State Circuits, IEEE Journal of*, vol. 35, pp. 512-526, 2000.

[5] J. Wang, Z. Ren, and C. T. C. Nguyen, "1.156-GHz self-aligned vibrating micromechanical disk resonator," *IEEE Transactions on UFFC*, vol. 51, pp. 1607-1628, 2004.

[6] S. A. Bhave, G. Di, R. Maboudian, and R. T. Howe, "Fully-differential poly-SiC Lame-mode resonator and checkerboard filter," in *Proceedings of MEMS 2005*. Miami, Florida, 2005, pp. 223-226.

[7] C. T. C. Nguyen, "Vibrating RF MEMS for next generation wireless applications," in *Proceedings, IEEE Custom integrated Circuits*. Orlando, Florida, 2004, pp. 257-264.

[8] S. Vengallatore, "Analysis of thermoelastic damping in laminated composite micromechanical beam resonators," *Journal of Micromechanics and Microengineering*, vol. 15, pp. 2398-2404, 2005.

[9] R. Sandberg, K. Molhave, A. Boisen, and W. Svendsen, "Effect of gold coating on the Q-factor of a resonant cantilever," *Journal of Micromechanics and Microengineering*, vol. 15, pp. 2249-2253, 2005.

[10] D. L. DeVoe, "Piezoelectric thin film micromechanical beam resonators," *Sensors and Actuators A-Physical*, vol. 88, pp. 263-272, 2001.

[11] M. Hara, J. Kuypers, T. Abe, and M. Esashi, "Surface micromachined AlN thin film 2 GHz resonator for CMOS integration," *Sensors and Actuators A-Physical*, vol. 117, pp. 211-216, 2005.

[12] G. Piazza, R. Abdolvand, G. K. Ho, and F. Ayazi, "Voltage-tunable piezoelectrically-transduced single-crystal silicon micromechanical resonators," *Sensors and Actuators a-Physical*, vol. 111, pp. 71-78, 2004.

[13] G. Piazza, P. J. Stephanou, J. M. Porter, M. B. J. Wijesundara, and A. P. Pisano, "Low motional resistance ring-shaped contour-mode aluminum nitride piezoelectric micromechanical resonators for UHF applications," in *Proceedings of MEMS 2005*. Miami, FL, 2005, pp. 20-23.

[14] S. Humad, R. Abdolvand, G. K. Ho, G. Piazza, and F. Ayazi, "High frequency micromechanical piezo-on-silicon block resonators," in *Proc. IEEE Int. Electron Devices Meeting*, 2003, pp. 39.3.1-39.3.4.

[15] L. H. Li, P. Kumar, L. Calhoun, and D. L. DeVoe, "Piezoelectric $Al_{0.3}Ga_{0.7}As$ longitudinal mode bar resonators," *Journal of Microelectromechanical Systems*, vol. 15, pp. 465-470, 2006.

[16] P. Kumar, L. H. Li, L. Calhoun, P. Boudreaux, and D. DeVoe, "Fabrication of piezoelectric $Al_{0.3}Ga_{0.7}As$ microstructures," *Sensors and Actuators A-Physical*, vol. 115, pp. 96-103, 2004.

[17] L. Li, "Piezoelectric Microbeam Resonators Based on Epitaxial $Al_{0.3}Ga_{0.7}As$ Films," *Dept. of Mechanical Engineering*, Ph. D Dissertation: University of Maryland at College Park, 2005.

[18] S. Adachi, "GaAs, AlAs, and $Al_xGa_{1-x}As$: Material parameters for use in research and device applications," *Journal of Applied Physics*, vol. 58, pp. R1-R29, 1985.

[19] K. Hjort, J. Soderkvist, and J. A. Schweitz, "Gallium-arsenide as a mechanical material," *Journal of Micromechanics and Microengineering*, vol. 4, pp. 1-13, 1994.

[20] J. Soderkvist and K. Hjort, "The piezoelectric effect of GaAs used for resonators and resonant sensors," *Journal of Micromechanics and Microengineering*, vol. 4, pp. 28-34, 1994.

[21] J. L. Leclercq, R. P. Ribas, J. M. Karam, and P. Viktorovitch, "III-V micromachined devices for microsystems," *Microelectronics Journal*, vol. 29, pp. 613-619, 1998.

[22] L. Li, P. Kumar, S. Kanakraju, and D. L. Devoe, "Piezoelectric AlGaAs bimorph microactuators," *Journal of Micromechanics and Microengineering*, vol. 16, pp. 1062-1066, 2006.

[23] C. T. C. Nguyen, "Vibrating RF MEMS Overview: Applications to Wireless Communications," in *Proceedings of MOEMS-MEMS 2005*. San Jose, CA, 2005, pp. 5715-201.

[24] J. F. Nye, *Physical properties of crystals their representation by tensors and matrices*. Oxford [Oxfordshire]: Clarendon Press, 1985.

[25] J. Yang, *An introduction to the theory of piezoelectricity*: Springer Science+Business Media, Inc., 2005.

[26] M. Garrigues, J. L. Leclercq, and P. Viktorovitch, "III-V semiconductor based MOEMS devices for optical telecommunications," *Microelectronic Engineering*, vol. 61-2, pp. 933-945, 2002.

[27] M. A. Dubois and P. Muralt, "Properties of aluminum nitride thin films for piezoelectric transducers and microwave filter applications," *Applied Physics Letters*, vol. 74, pp. 3032-3034, 1999.

[28] A. Dehe, K. Fricke, K. Mutamba, and H. L. Hartnagel, "A piezoresistive GaAs pressure sensor with GaAs/AlGaAs membrane technology," *Journal of Micromechanics and Microengineering*, vol. 5, pp. 139-142, 1995.

[29] K. Fobelets, R. Vounckx, and G. Borghs, "A GaAs pressure sensor-based on resonant-tunneling diodes," *Journal of Micromechanics and Microengineering*, vol. 4, pp. 123-128, 1994.

[30] C. T. C. Nguyen, "Vibrating RF MEMS technology: fuel for an integrated micromechanical circuit revolution?," in *Proceedings, Transducers'05*, vol. 1. Seoul, Korea, 2005, pp. 243-246.

[31] S. Reid, G. Cagnoli, D. R. M. Crooks, J. Hough, P. Murray, S. Rowan, M. M. Fejer, R. Route, and S. Zappe, "Mechanical dissipation in silicon flexures," *Physics Letters A*, vol. 351, pp. 205-211, 2006.

[32] A. H. Nayfeh and M. I. Younis, "Modeling and simulations of thermoelastic damping in microplates," *Journal of Micromechanics and Microengineering*, vol. 14, pp. 1711-1717, 2004.

[33] R. Lifshitz and M. L. Roukes, "Thermoelastic damping in micro- and nanomechanical systems," *Physical Review B*, vol. 61, pp. 5600-5609, 2000.

[34] J. L. Yang, T. Ono, and M. Esashi, "Energy dissipation in submicrometer thick single-crystal silicon cantilevers," *Journal of Microelectromechanical Systems*, vol. 11, pp. 775-783, 2002.

[35] Z. Zhang, P. C. Hammel, M. Midzor, M. L. Roukes, and J. R. Childress, "Ferromagnetic resonance force microscopy on microscopic cobalt single layer films," *Applied Physics Letters*, vol. 73, pp. 2036-2038, 1998.

[36] X. Zhang and W. C. Tang, "Viscous air damping in laterally driven microresonators," *Sensors and Materials*, vol. 7, pp. 415-430, 1995.

[37] Y. J. J. Yang and P. C. Yen, "An efficient macromodeling methodology for lateral air damping effects," *Journal of Microelectromechanical Systems*, vol. 14, pp. 812-828, 2005.

[38] W. J. Ye, X. Wang, W. Hemmert, D. Freeman, and J. White, "Air damping in laterally oscillating microresonators: A numerical and experimental study," *Journal of Microelectromechanical Systems*, vol. 12, pp. 557-566, 2003.

[39] T. Veijola and M. Turowski, "Compact damping models for laterally moving microstructures with gas-rarefaction effects," *Journal of Microelectromechanical Systems*, vol. 10, pp. 263-273, 2001.

[40] Y. H. Cho, A. P. Pisano, and R. T. Howe, "Viscous damping model for laterally oscillating microstructures," *Journal of Microelectromechanical Systems*, vol. 3, pp. 81-87, 1994.

[41] Z. L. Hao, A. Erbil, and F. Ayazi, "An analytical model for support loss in micromachined beam resonators with in-plane flexural vibrations," *Sensors and Actuators A-Physical*, vol. 109, pp. 156-164, 2003.

[42] M. C. Cross and R. Lifshitz, "Elastic wave transmission at an abrupt junction in a thin plate with application to heat transport and vibrations in mesoscopic systems," *Physical Review B*, vol. 64, pp. art.-085324, 2001.

[43] A. A. Shabana, *Vibration of Discrete and Continous Systems*: Springer, 1997.

[44] R. A. Johnson, *Mechanical Filters in Electronics*: New York: Wiley, 1983.

[45] B. H. Houston, D. M. Photiadis, M. H. Marcus, J. A. Bucaro, X. Liu, and J. F. Vignola, "Thermoelastic loss in microscale oscillators," *Applied Physics Letters*, vol. 80, pp. 1300-1302, 2002.

[46] J. E. Bishop and V. K. Kinra, "Thermoelastic damping of a laminated beam in flexure and extension," *Journal of Reinforced Plastics and Composites*, vol. 12, pp. 210-226, 1993.

[47] B. H. Houston, D. M. Photiadis, J. F. Vignola, M. H. Marcus, X. Liu, D. Czaplewski, L. Sekaric, J. Butler, P. Pehrsson, and J. A. Bucaro, "Loss due to transverse thermoelastic currents in microscale resonators," *Materials Science and Engineering A-Structural Materials Properties Microstructure and Processing*, vol. 370, pp. 407-411, 2004.

[48] L. Li, P. Kumar, L. Calhoun, and D. L. DeVoe, "Piezoelectric bimorph transducers based on single crystal Al/sub 0.3/Ga/sub 0.7/As films," 2005.

[49] M. E. Frerking, *Crystal oscillator design and temperature compensation*: Van Nostrand, 1978.

[50] Y. D. Kim, K. H. Sunwoo, S. C. Sul, J. H. Lee, D. H. Kim, I. S. Song, S. H. Choa, and J. G. Yook, "Highly miniaturized RF bandpass filter based on thin-film bulk acoustic-wave resonator for 5-GHz-band application," *IEEE Transactions on Microwave Theory and Techniques*, vol. 54, pp. 1218-1228, 2006.

[51] Y. W. Lin, S. Lee, S. S. Li, Y. Xie, Z. Y. Ren, and C. T. C. Nguyen, "Series-resonant VHF micromechanical resonator reference oscillators," *IEEE Journal of Solid-State Circuits*, vol. 39, pp. 2477-2491, 2004.

[52] B. Piekarski, D. DeVoe, M. Dubey, R. Kaul, and J. Conrad, "Surface micromachined piezoelectric resonant beam filters," *Sensors and Actuators A: Physical*, vol. 91, pp. 313-320, 2001.

[53] S. Lee and C. T. C. Nguyen, "Mechanically-coupled micromechanical resonator arrays for improved phase noise," in *IEEE Int. UFFC 50th Anniv. Joint conf.* Montreal, Canada, 2004, pp. 280-286.

[54] M. U. Demirci, M. A. Abdelmoneum, and C. T. C. Nguyen, "Mechanically corner-coupled square microresonator array for reduced series motional resistance," in *Transducers'03*, vol. 2. Seoul, Korea, 2003, pp. 955-958